4-2022

Air-Deflected Microfluidic Chip for Characterization of Fluid-Structure Interactions

Chad ten Pas
cwt1415@rit.edu

Recommended Citation

ten Pas, Chad, "Air-Deflected Microfluidic Chip for Characterization of Fluid-Structure Interactions" (2022). Thesis. Rochester Institute of Technology. Accessed from

Air-Deflected Microfluidic Chip for Characterization of Fluid-Structure Interactions

by

Chad ten Pas

A Thesis Submitted in Partial Fulfillment of the Requirements for the Degree of Master of Science in Mechanical Engineering

Supervised by

Assistant Professor Ke Du, Ph.D.
Department of Mechanical Engineering
Kate Gleason College of Engineering
Rochester Institute of Technology
Rochester, NY
April 2022

Approved by:

____ Date:_____________
Dr. Ke Du, Assistant Professor
Thesis Advisor, Department of Mechanical Engineering

____ Date:_____________
Dr. Kathleen Lamkin-Kennard, Associate Professor
Committee Member, Department of Mechanical Engineering

____ Date:_____________
Dr. Ruo-Qian (Roger) Wang, Assistant Professor
Committee Member, Department of Civil and Environmental Engineering
Rutgers, The State University of New Jersey

____ Date:_____________
Dr. Michael Schrlau, Associate Professor & Graduate Director
Department Representative, Department of Mechanical Engineering

Abstract

Millions of people suffer from dentinal pain each year caused by a pressure change and fluid shear in the dentin tubule and nerve pulp system. Dentin is made up of mostly hydroxyapatite, a hard and opaque material. In-situ characterization is extremely challenging because of the tubules that run through are high-aspect ratio micropores with a feature size of 1-2 µm. Current studies have proven that various methods can be deployed to fabricate microscale geometry using PDMS. The most used methods are three-dimensional stereolithography, fused deposited material (FDM), 3D printed sacrificial mold, FDM 3D printed molds and soft lithography molding from the existing literature. This study simplifies dentin tubules by enlarging and creating a planar case for analysis. The chip geometry investigated consist of three 2 mm by 2 mm by 50 mm parallel channels separated by thin walls of 500 µm, 750 µm, and 1000 µm. The central channel is fitted with a glass capillary and holds liquid. The two outer channels are air pressure channels. The fabrication process is highlighted in this study and utilizes 3D FDM and 3D stereolithography (SLA) printing, negative molding of polydimethylsiloxane (PDMS), spin coating PDMS to create a 1 mm layer, and PDMS-PDMS bonding for chip completion. Pressure is applied to the completed chips in known increments and the dynamic response of the chip is recorded through image capture and processing. The experiments show a sequential, three process response. A strong linear correlation was found between steady state liquid surface height and applied pressure. The theoretical model can fit well the second and third processes of the response by ascertaining the initial height of the second process. The oversimplification and theoretical simulation results lay the groundwork for microfluidic devices that more closely model dentin tube structure, such as the polyvinyl alcohol (PVA) fibers positioned in an array to be tested in a similar fashion to the device in this study.

Table of Contents

List of Figures

List of Tables

Nomenclature

The nomenclature used in this study is listed and described below.

DIW = direct ink writing

FDM = fused deposited material

FSI = fluid-structure interaction

ITO = indium tin oxide

MEMS = micro-electro-mechanical system

PDMS = polydimethylsiloxane

PLA = polylactic acid

PPM = planar pneumatic microvalve

PVA = polyvinyl alcohol

SLA = stereolithography

m- = “milli- “

mm = “millimeter”

ms = “millisecond’

µ- = “micro- “

µm = “micrometer” or “micron”

ρ = fluid density

u = fluid velocity

g = acceleration due to gravity

t = time

z = fluid surface level

h_L = head loss in device

P = pressure

A = cross-sectional area

P_C = deformation coefficient for pipe law

α = material & shape coefficient for pipe law

μ = dynamic fluid viscosity

f = coefficient of friction

L = length of channel

1.0 Problem Introduction

Dentine hypersensitivity is bothering over 3 million people each year in the United States. Thermal stimuli can cause the deformation of the dentin tubules and pressure change in the pulp chamber. The fundamental understanding of the dentin tubules deformation will be the key to advance the treatment of dentin hypersensitivity. However, 70% of the dentin is mineral hydroxyapatite, which is a hard and opaque material that is difficult to characterize. Dentin tubules are high-aspect ratio micropores with a feature size of 1-2 µm, making the in-situ characterization extremely challenging.

The field of microfluidics has been heavily facilitated using elastic polymers, the most widely used, being polydimethylsiloxane (PDMS). With PDMS, microscale geometry can be fabricated using various methods such as soft lithography molding, fused deposited material (FDM) 3D printing molds, FDM 3D printed sacrificial mold, and 3D stereolithography (SLA). The high elasticity of PDMS allows an exaggerated interface between fluid and structure. This exaggerated interface can be a novel approach to defining fluid-structure interactions (FSI) in microfluidics. This study investigates, both experimentally and theoretically, long high aspect ratio channels with thin wall geometry of PDMS subject to a range of known reservoir pressures.

1.1 Introduction to Tooth Anatomy: Dentin Tubules

Dentin refers to the hard, porous, and mineralized part of the tooth, a connective tissue majorly made of collagen type 1 fibrils coated with hydroxyapatite. Besides the type 1 collagen, dentin has types 3,5 and 6 collagens, proteins, as well as proteoglycans as minor components [1]. Pulp odontoblasts are responsible for the matrix formation; they secrete collagen at dentin-enamel junction before retreating centripetally. This gives primary and secondary dentin their tubular nature [2,3]. However, the tertiary dentin lacks the regular tubular form because it is a consequence of noxious stimuli. The tubular nature is also a product of the larger circumference on the peripheral part of the crown than that of the final pulp chamber; thus, odontoblasts are closely linked in forming inter tubular dentin.

The number of dentinal tubules varies between 15000 at the dentin-enamel junction to 45000 tubules per mm^2 at the pulp. Narrowing of the tubules often can result from deposition of intratubular dentin within the tubules. Dimensions of the tubules vary depending on the location [3]; the largest diameter (2.5 μm) is found at the pulp, whereas the smallest dimension is at the dentin-enamel junction (about 0.9 μm in diameter) [1,4]. While the tubular structure gives dentin its porosity, its level of permeability is determined by the location on the tooth and the number of available patent tubules. Normally, the enamel protects the dentin from the oral cavity and is only exposed by factors like cavities, trauma or periodontal procedures which alter the integrity of the enamel [1]. This creates a diffusion channel from the pulp’s surface, consequently allowing microorganism and other noxious substances to diffuse across the dentin causing reactions.

1.2 Introduction to Tooth Stress: Shear fluid Pain Theory

Fluid flow in dentinal microtubules results from noxious thermal or mechanical stimuli applied to the dentin. It is the fluid flowing through the dentin that triggers shear stress on interdental nerve endings and consequent excitation of pulpal mechanoreceptors leading to dental pain [5]. In an intact tooth, there is no exchange of fluid between the oral cavity and the dentin. However, normal sensitivity can be observed by discomfort experienced when eating hot or very cold foods; convection currents generated in tubular fluids can cause shear stress on nerve fibers, leading to pain. Loss of the protection from the enamel leaves the dentin exposed to more shear stress as fluid moves between the dentin and the oral cavity.

Pulpal fluid pressure, therefore, plays a crucial hydrodynamic role in determining dentin sensitivity by influencing the rate of fluid flow. Increased pressure causes rapid outward movement of the fluid under stimulus. The rise in pulpal pressure is even higher when fluid flows inward. Ideally, any factors that affect rate of fluid flow like volume of the fluid, diameter of the tubule, viscosity of the fluid, and length of the tubule can greatly alter sensitivity according to Poiseuille’s equation. For instance, assuming that tubular fluid viscosity remains constant, a tubule reduced by half will have fluid flow increased by over 32 times when compared to a normal tubule. This could be the reason for higher sensitivity on deeper cavities [4] since the dentin tubule diameter, on average, are close to three times as large near the pulp than the dentin-enamel junction . Studies by Lin et al. [5] also established that dimensions of biological structures, odontoblastic process motion, velocity of dentinal fluid, and viscosity had an impact on shear stress. Therefore, current treatment strategies are directed desensitization of the dentin by use of pastes and resin-bonding for restoration.

1.3 Introduction to Deformable Microfluidics

With continued growth in microfluidics technology in several aspects of molecular and other biological fields, more low-cost point of care biomedical devices will be needed. Exploring deformable microfluidics may, thus, offer unique advantages, ranging from recyclability, affordability to higher efficiency and convenience [6]. Current research recognizes the widespread use of polydimethylsiloxane (PDMS) as the preferred substrate in manufacturing of analytical systems. Furthermore, PDMS has also been applied in fabrication of other microfluidic devices as an elastomer in contemporary engineering [6,7] and in biosensors and bioelectronics [8–10], but are used without characterizing the geometries of these devices The faster processing, simple modeling, low cost, and visual clearness are some of the properties that make PDMS more suited for microfluidics [11].

With increased shear stress being particularly problematic due to the dental sensitivity and pain induced, more innovative ways need to be onboarded to help in the treatment. Some recent studies have evaluated the hydrodynamic behavior of certain deformable objects with respect to the deformability from droplets and to cells in dentin tubules [12]. The study indicated that mechanical properties like size and viscosity of the deformable objects were related to the level of hydrodynamic resistance [13]. This implies that use of microfluidics could potentially solve the problem of shear stress on the dentin and improve the treatment outcomes. A study by Khanafer et al. [12,14] showed the existence of a link between mechanical effects on cross-linking agents and pre-polymer bases. Depending on the mixing ratios, researchers recorded a change in elasticity, something that could be related to the resistance observed in the PDMS [2,15]. This property confers it with a greater mechanical strain in response to a little stimulus or pressure.

1.4 Theoretical Model

The Air Deflected Microfluidic Chip (ADMC) begins to approach the problem stated above about dentin tubes by making a larger, simplified planar case of the scenario. To help understand the dynamics of fluid-structure interaction and to aid future device design, a theoretical model was developed to compare to experimental results. The model was developed and simulated by Ruo-Qian (Roger) Wang and his group at Rutgers University. Since elasticity of PDMS does not match that of dentin, a theoretical model focused on the fluid dynamics of the chip was developed. To simplify the calculations, the model can be separated into two sections – the pressurized channel filled with liquid and the glass capillary at the end of the channel. Since the total fluid is conserved within our device, we can assume that the volumetric flow through each section is equal. Thus,

$$u_I A_I = u_T A_T \ , \qquad (1)$$

where A_I and A_T are the cross-sectional areas, and u_I and u_T are the fluid velocities. The subscripts I and T correspond to the horizontal central liquid channel and the vertical glass capillary, respectively. Additionally, if we apply the unsteady Bernoulli equation to the device:

$$\int_I^T \rho \frac{\partial u}{\partial t} ds + \left(P + \frac{1}{2}\rho u^2 + \rho g z\right)_T - \left(P + \frac{1}{2}\rho u^2 + \rho g z\right)_I + \rho g h_L = 0, \qquad (2)$$

where ρ is the fluid density, u is the velocity, t is time, P is the pressure, g is acceleration due to gravity, z is the height of the fluid, h_L is the head loss in the flow, which accounts for any major and minor losses in the device [16]. The height of the horizontal liquid channel does not vary and can be referenced as $z_I = 0$. The free surface of the liquid in the vertical glass capillary is z_T, which means that the surface is exposed to atmospheric pressure. A schematic with respective parameters is labeled in Figure 1(a).

We can describe the pressure difference across the inside and outside of the horizontal liquid channel as transmural pressure. Several tube laws are proposed in the literature [17,18] and the most popular one used in flexible tubes is used:

$$P_E - P_I = P_C\left[\left(\frac{A_I}{A_0}\right)^{\alpha} - 1\right], \qquad (3)$$

where P_E and P_I are the pressure outside and inside the horizontal liquid channel as shown in Figure 1(b), A_I was defined earlier as the cross-sectional area of the liquid channel, A_0 is the initial cross-sectional area of the liquid channel, P_C is a deformation coefficient, and α is a shape and materials coefficient of the channel.

The Reynold’s number is assumed to be lower than 2000, so we use the laminar Darcy-Weisbach equation to approximate the head losses the device by combining losses in both the horizontal liquid channel and the vertical glass capillary:

$$h_L = f_I \frac{\mu L}{\rho g A_I} u_I + f_T \frac{\mu\, z_T}{\rho g A_T} u_T = \left(\frac{f_I L u_I}{A_I} + \frac{f_T\, z_T u_T}{A_T}\right)\frac{\mu}{\rho g}, \qquad (4)$$

where f_I and f_T are coefficients of friction, μ is the fluid viscosity, and L is the length of the horizontal liquid channel. Rearrange equation (1) to

$$u_T = u_T \frac{A_I}{A_T}, \qquad (5)$$

and plug into equation (4) to get in terms of only the velocity of the horizonal liquid channel:

$$h_L = \left(\frac{f_I L\, u_I}{A_I} + \frac{f_T\, z_T}{A_T} u_I \frac{A_I}{A_T}\right)\frac{\mu}{\rho g} = \left(\frac{f_I L}{A_I} + \frac{f_T\, z_T}{A_T}\frac{A_I}{A_T}\right)\frac{\mu\, u_I}{\rho g}. \qquad (6)$$

If we plug equations (3) and (6) into (2), the system becomes:

$$\rho \frac{\partial u_I}{\partial t} L + \rho \frac{\partial u_T}{\partial t} z + \left(\frac{1}{2}\rho u_T^2 + \rho g z_T\right) - \left(\frac{1}{2}\rho u_I^2 + P_I\right) + \left(\frac{f_I L}{A_I} + \frac{f_T\, z_T}{A_T}\frac{A_I}{A_T}\right)\frac{\mu\, u_I}{\rho g} = 0. \qquad (7)$$

If we assume the friction factors are equal for PDMS and the glass capillary tube:

$$f = f_I = f_T.$$

To solve this system of equations we will normalize the system of equations so that an implicit solver can be used equations (8 – 11):

$$U_I A = \frac{A_V}{A_0} U_T, \qquad (8)$$

$$\frac{\partial U_I}{\partial T} + \frac{\partial U_T}{\partial T} Z + \frac{1}{2} U_T^2 + Z - (\Delta + \beta A^{\alpha}) - \frac{1}{2} U_I^2 + f\left(\frac{1}{A} + \frac{z_T A}{\left(\frac{A_T}{A_0}\right)^2}\right)\gamma U_I = 0, \qquad (9)$$

$$U_T = \frac{\partial Z}{\partial T}, \qquad (10)$$

$$\frac{\partial A}{\partial T} = -A U_I, \qquad (11)$$

where the coefficients are:

$$U_I = \frac{u_I}{\sqrt{gL}}, \qquad A = \frac{A_I}{A_0}, \qquad T = \sqrt{\frac{g}{L}}\,t, \qquad Z = \frac{z_T}{L},$$

$$\Delta = \frac{P_C+P_E}{\rho g L}, \qquad \beta = \frac{P_C}{\rho g L}, \qquad \gamma = \frac{\nu L^{\frac{1}{2}}}{g^{\frac{1}{2}} A_0}.$$

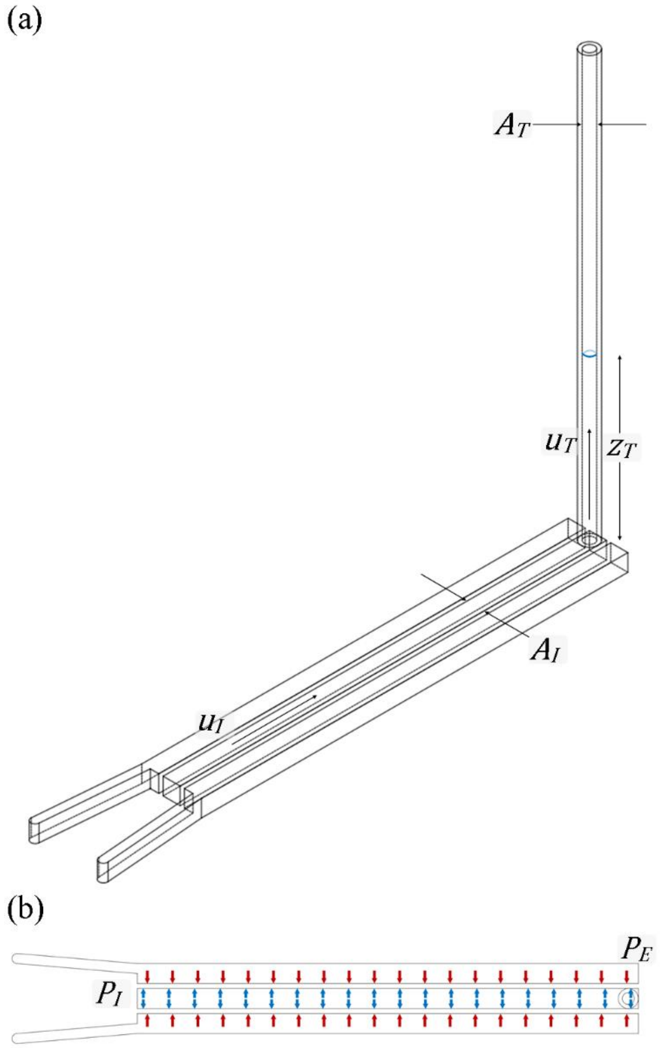

Figure 1. Schematic of theoretical model. (a) Isometric view of internal channels and glass capillary. (b) Top view of internal channels with symbolic pressures.

Using this system of equations and MATLAB, the theoretical model can be simulated. The best function for this is the ode15i function as it has implicit function solving capability. There was assumed to be no deformation and an initial velocity of the fluid equal to zero at t = 0.

2.0 Literature Review

The use of polymer is wildly spread in daily human lives, with synthetic polymers being one of the premium discoveries of mankind. Synthetic polymers are specifically designed macromolecules forming some of the fundamental bases applied in the engineering field. The adoption of microfluidic technology gained eminence in the 1908s [19]. To date, microfluidics has been deployed in various engineering and science fields, from aerospace to biochemistry engineering technology. Different scholars have recognized the wide adoption of polydimethylsiloxane (PDMS) as a substrate material for the industrial build-up of micro-scale, total analysis systems and lab-on-a-chip [20,21]. Specifically, the extensive fabrication of microfluidic devices in the contemporary engineering and science fields has been based on PDMS as the most frequently used elastomer. According to Sollier et al. [22], the wide use of PDMS in microfluidic systems is attributed to its physical and chemical properties. To strengthen the assertions of Sollier et al. [22], Johnston et al. [23] underscore that the extensive use of PDMS in microfluidic fabrication can be linked to its fast, simple molding, low cost, and its visual clearness through the visible spectrum. In agreement with other scholars, McDonald and Whitesides [21] further add that the suitability of PDMS for the soft lithography process can be credited to its ability to replicate microscale features and low shrinkage rates. These elements give PDMS a primary advantage as the most preferred materials for microfluidic systems over other substrate materials.

2.1 Properties of PDMS

Although PDMS substrate has been widely deployed in integrating microfluidics technology and other fields like engineering biology and chemistry (that has seen computational approach to edge detection [24], use of subpixel techniques to measure displacement and vibrations [25]), it has certain significant limitations. According to Johnston et al. [26], PDMS structures normally distort when an outside force is applied, such as pressure, flow diversion or in-flow stream restriction. Moreover, Sollier et al. [22] emphasize that PDMS use in some high pressure and chemical applications is restricted due to its low hardness and poor chemical compatibility. For example, the use of organic solvent can result in swelling [22]. Equally, Berthier et al. [27] confirm the findings of these scholars and add that PDMS as substrate material has features that have several negative effects on cell-based biological tests. The adverse effects of PDMS on cell-based microfluidic systems have caused a great ideological disparity between microfluidic system design engineers and biologists over the ideal material selection features for microdevice fabrication. Although the use of PDMS in micro-device fabrication has been widely adopted by microfluidic engineers (due to its attractive properties), increased research findings from biologists has highlighted possible spurious effects attributed to the use of PDMS microdevices in cell study and culture [28,29]. However, despite the controversial assertions by scholars from these different fields, the advantages of PDMS microdevices significantly overshadow their shortcomings for many applications.

Johnston et al. [23] posit that the unique advantages offered by PDMS over more old-style substrate materials like hard polymers, silicon, and glass, is due to its elasticity validated by the micro-electro-mechanical systems (MEMS) and microfluidic systems. In agreement with Sollier et al. [22], Johnston et al. [23] postulate that microfluidic engineers are facilitating flexible microstructure within composite structures to take advantage of the low hardness of the relative deformability of the low hardness PDMS. Examples of microfluidic engineering devices based on this unique feature of PDMS include flexible, adaptable fluid lenses [30], mechanically modifiable PDMS devices for cell trapping [31], flexible micropillar arrays for biological force measurements [32], solid hydraulic operated PDMS microvalves [33], and micropumps using elastomeric displacement amplification [34].

Like its low hardness, different specific scientific investigations on the mechanical properties of PDMS have been based on elasticity. Precise applications have formed the basis of these research works. Such applications include the nonlinear and biomedical behavior of PDMS in modified and standard compositions [35,36], material elasticity for accelerometers [37], and thin embrace for sensors [38]. Research findings have determined that Young's modulus of PDMS films can change from bulk behavior to dimension-dependent behavior [39]. Specifically, these scholars determined that this change is from above 200 μm thickness to below 200 μm [37]. In agreement with these earlier findings, Liu et al. [40] and Koschwanez et al. [41] determined that the properties of the resulting material can significantly be influenced by spin coating films for thin PDMS. Therefore, this measurement reliance on thin films during the fabrication of layers can be attributed to polymer chain reordering during the spin coating process.

Khanafer et al. [12] studied the mechanical effects of varying cross-linking agents and pre-polymer base relationships. Increasing the cross-linker to PDMS base mixing ratio caused an increase in the elastic modulus. Most manufacturers have recommended a mix ratio of 10:1 for PDMS microstructured components employed in microfluidic applications. Moreover, the thickness of these fabricated microstructures is always greater than 200 μm [39]. Johnston et al. [23] observed a linear correlation between curing temperature and Young's modulus as shown in Figure 2. The findings by these earlier scholars validate the necessity to understand the processing-reliant disparity in mechanical properties of the PDMS for efficient and accurate microengineering and microfluidics application.

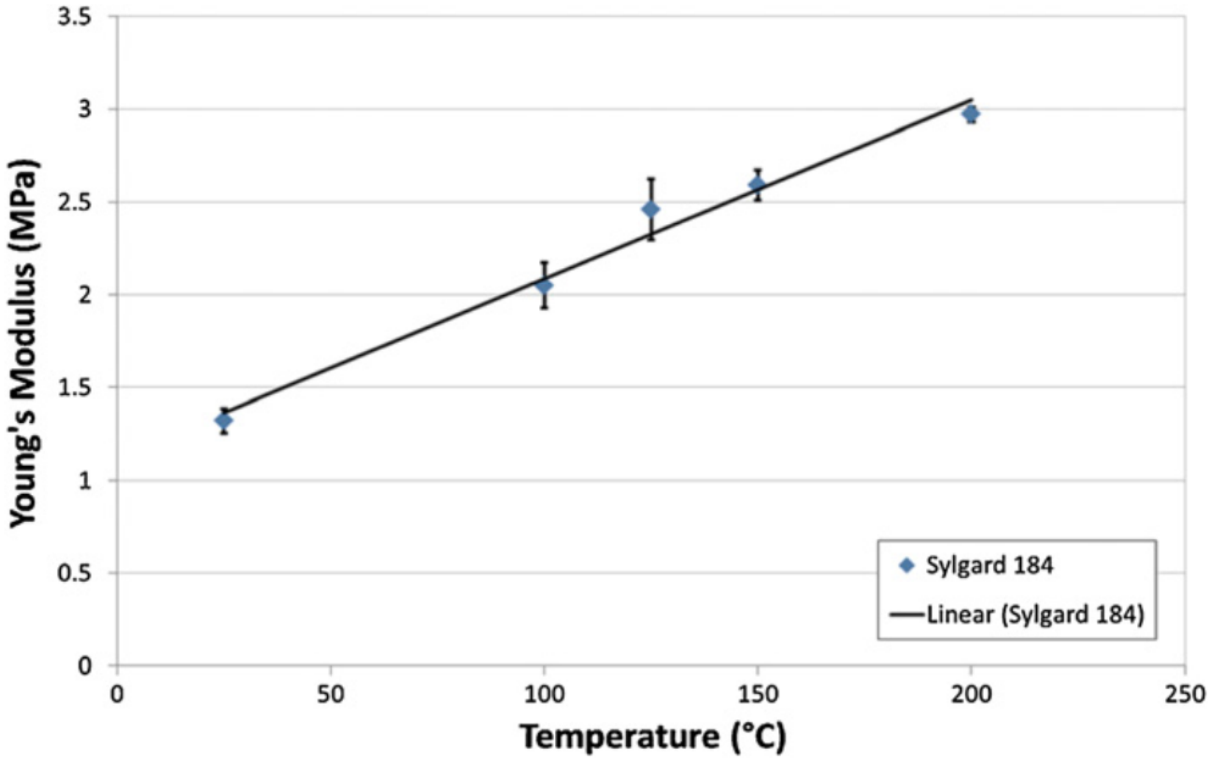

Figure 2. Correlation between curing temperature of Sylgard 184 and the resultant Young's modulus (Source: Johnston et al. [23] and licensed under CC BY-SA 4.0)

Table 1. Summary of bulk properties of 10:1 ratio PDMS (source Johnston et al. [23] and licensed under CC BY-SA 4.0)

Temperature (°C)	*E* (MPa)	UTS (MPa)	Hardness (Shore A)	Ec (MPa)	UCS (MPa)	*G* (MPa)	*K* (GPa)
25	1.32 ± 0.07	5.13 ± 0.55	43.8 ± 0.76	186.9 ± 5.39	51.7 ± 9.60	0.44 ± 0.02	2.20 ± 0.11
100	2.05 ± 0.12	6.25 ± 0.84	48.3 ± 0.65	148.9 ± 5.47	40.1 ± 4.30	0.68 ± 0.04	3.42 ± 0.17
125	2.46 ± 0.16	7.65 ± 0.27	49.8 ± 0.45	137.7 ± 2.82	36.8 ± 3.84	0.82 ± 0.05	4.11 ± 0.20
150	2.59 ± 0.08	5.24 ± 0.82	52.8 ± 0.73	136.1 ± 2.68	28.4 ± 4.46	0.86 ± 0.03	4.32 ± 0.22
200	2.97 ± 0.04	3.51 ± 1.11	54.0 ± 0.08	117.8 ± 2.17	31.4 ± 2.04	0.99 ± 0.01	4.95 ± 0.25

2.2 Three-Dimensional Microfluidics in PDMS

Rapid prototyping of microfluidic devices has deployed the soft lithography process as the standard fabrication methodology [42]. Nonetheless, the typical process continued to use photolithography as the main step, the flexibility of soft lithography notwithstanding. Richmond and Tompkins [13] noted that the whole soft lithography process is extremely expensive for smaller research facilities and attributed to photolithography. Therefore, these scholars replaced the cleanroom facilities essential for photolithography with an inexpensive three-dimensional (3D) printer to describe a variant of soft lithography [43]. This research determined that while all the material advantages of PDMS (including its mechanical properties), variation permitted fully-3D microfluidic devices at a cost variation [43]. Another advantage established by these scholars that agrees with the earlier findings of Eddings et al. [44] is the replacement of plasma bonding by PDMS, which had enough strength for microfluidic flow [43].

Fabrications by Shankles et al. [45] and Felton et al. [46] incorporated a 3D-printed master to replace photolithographic master to create soft lithography masters while following the same process. Although these approaches only deployed a single surface of the printed object as a master, Richmond and Tompkins [13] created fully three-dimensional geometries by using surface relief from multiple surfaces during the same molding step, thus treating the entire process as three-dimensional (Figure 3).

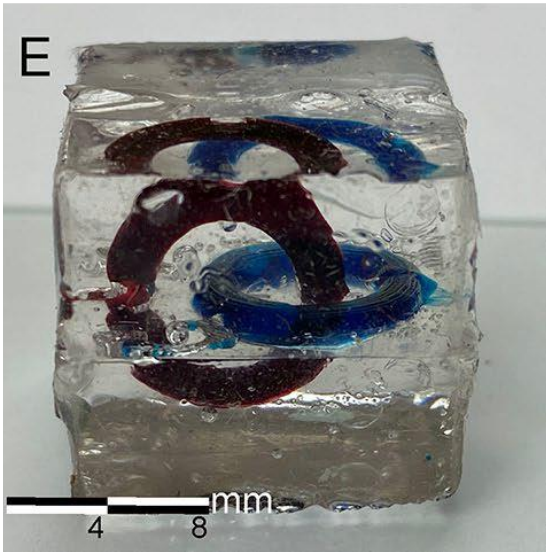

Figure 3. Three-dimensional geometry in PDMS (Source: Richmond and Tompkins [13] and reused with permission from Springer Nature).

Different scholars have regularly deployed three-dimensional microfluidic systems in their studies. While Guo et al. [47] deployed 3D microfluidic systems in the study of nanotube microfibers, Lyu et al. [48] and Lin et al. [49] used the same technique in cell sorting and protein cross-linking, respectively. Similarly, 3D microfluidic systems have been used in the study of magnetic droplets by He et al. [50], droplet formation by Wang et al. [51] and Jeyhani et al. [52], coaxial flow by Rodriguez-Trujillo et al. [53], and flow-focusing by Shivhare et al. [54]. The fabrication of 3D microfluidic devices has been attained using different elements. While Su et al. [55] used direct 3D printing, Goh and Hashimoto [56] first used 3D printing and later fabricated 3D microchannels using helical and overhand features [57]. Equally, commercial tee connectors and glass capillaries have been used. Nonetheless, there is a need to have a final product that is not solely made of PDMS, in addition to some compromise of expensive equipment, the fabrication methods deployed notwithstanding. However, to produce a single PDMS microfluidic device, Richmond and Tompkins [13] managed to formulate a 3D molding method that only used PDMS casting and a relatively cheap extrusion of 3D printers.

Scholars, such as Waheed et al. [58] and Morgan et al. [59], made tremendous progress in deploying fully 3D printed microfluidics. However, the existing materials still fail to equal the chemical and optical properties of monolithic PDMS. Kolesky et al. [60] and Femmer et al. [61] fabricated a three-dimensional PDMS printer for bioprinting. However, the printer developed by Femmer et al. [61] was designed as stereolithography, and the produced print had no voids. Like 3D PDMS printers, other scholars such as Bhattacharjee et al. [62] have strived to produce new resins with similar properties as PDMS. Interestingly, no resin can fully take the place of PDMS. The three-dimensional fluid flow environment is significant as it improves visibility. Although most contemporary research utilizes 3D microfluidics mainly at the millimeter scale, as highlighted by He et al. [47] and Lin et al. [49], high tech knowledge and expensive equipment are needed to manufacture this type of work. However, the proposal of Richmond and Tompkins [13] simplifies the design and creation of 3D microfluidics applications for most research laboratories. Therefore, all these research works by the earlier scholars highlight the unending tremendous progress in microfluidics device fabrication and engineering.

2.3 Sacrificial Molding

Conventional microfluidic device fabrication methods utilize duplication molding to formulate two-dimensional (2D) microchannels geometry that matches photolithography modeled molds [63]. Interestingly, Qin et al. [64] determined that detailed arrangement and strenuous heaping of several matrix-consisting layers of complementary segments would be necessary by replicating soft lithography and molding. Howell Jr. et al. [65] and Tóth et al. [66] agreed with McDonald et al. [63] and underscored that this leads to the absolute assembly of the 3D microfluidic devices. Numerous approaches, including sintering, molding, and etching, may be joined to produce complex 3D structures by considering demanding alignment [67]. Recently, 3D printing has been confirmed to engineer 3D microchannel geometry harbored by microfluidic devices. Earlier research works have determined that models of 3D printing proficient in generating a complete device that is microfluidic comprise of fused deposition modeling (FDM) [68,69], polymer jet printing [70], and stereolithography (SLA) [71]. Comparatively, microfluidic devices are capable of being engineered by microscale mold evacuation in various polymer matrices. Goh and Hashimoto [56] agree that this procedure is recognized as sacrificial molding. Considering this technique, eutectic metal [72], acrylonitrile butadienestyrene (ABS) [73], aqueous-based or organic solutions [74] and substrates that are sugar-based [75] have proven to be indispensable sacrificial materials in the formation of organized dimension microchannels. Therefore, complex 3D characteristics of sacrificial molds like the herringbones that are staggered to fabricate micromixers implanted in the microchannels have been patterned by FDM 3D printing [56].

Regardless of all effective sacrificial molding demonstrations to yield matrix-filled microchannels, Goh and Hashimoto [57] underscore that the important designs achieved were still restricted to the conferred geometry by the sacrificial mold. Equally, these scholars note that the geometry printed of the sacrificial mold may be inhibited by the ability of the production handling instrument of the mold [57]. Sacrificial materials fabrication has been confirmed through FDM 3D printers [43] and direct ink writing (DIW). Consequently, According to Goh and Hashimoto [57], materials for liquid sacrificial are patterned directly with DIW 3D printers in other matrices, and therefore obtaining a vigorous sacrificial molds' 3D structure is impossible. The elementary principle of FDM 3D printing includes object fabrication in the vertical dimension following a layered fashion to achieve a final structure. The external surface of all earlier structures printed prints a successive layer of material extruded on the support.

Conversely, a remarkable challenge becomes evident after a fabricated design comprises suspended 3D geometries in space. 3D microchannels features such as helix or overhangs would prove challenging to make while highlighting microchannels of fabrication through sacrificial molding. A preceding layer beneath the area where the features of the sacrificial material would be printed will be required by the suspended features. Therefore, the preceding layer is detached to disclose the overhang features. Figure 4 shows the process of dual sacrificial molding.

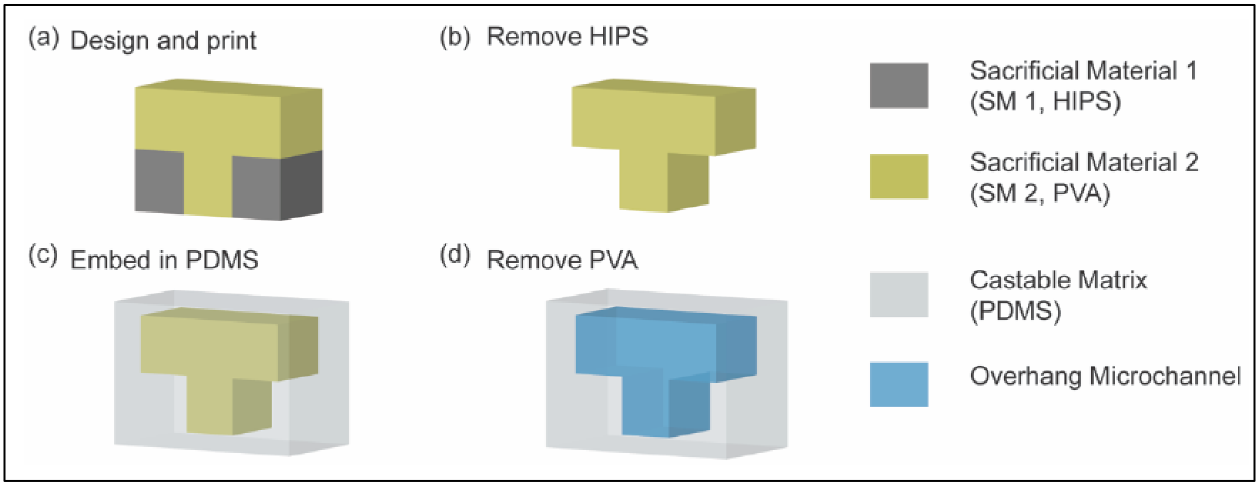

Figure 4. Dual sacrificial molding process (Source: Goh and Hashimoto [57] and licensed under CC BY-SA 4.0)

Presently, microchannels produced with helical and overhang characteristics by sacrificial molding are broadly still puzzling. This necessitates the usage of supplementary tools. For instance, Guérin et al. [76] used a mold prepared by fugitive ink dispensation onto a rotating template to fabricate helix structures that would convert into microchannels of helical after sacrificial molding in a matrix of epoxy. In comparison to Guérin et al. [76], Hwang et al. [77] used a mold similar to the helical structure to physically pull out of the castable matrix after production by polymer jetting. Alternately, heating and handling material to the preferred form by hand can be employed to form overhang structures during post-fabrication [73]. Regardless of those procedures, 3D microchannels production by sacrificial molding has been restricted by the limitation of supple approaches to generate subjective 3D molds shape applying strong sacrificial materials.

3.0 Fabrication of the ADMC

The fabrication of the negative mold design took three stages of evolution to overcome obstacles faced during development. The outcome is a device that can be fabricated with high consistency, but at a cost resulting in a complex fabrication process.

First negative mold design and chip fabrication:

The first negative mold design incorporated several geometrical variations, the first being the void gap between the channels and the second is varying the length of the pressure channels adjacent to the central channel. The void gap corresponds to a thin wall between the channels after the device is casted and chosen for the first design were 400 µm, 450 µm and 500 µm. The pressure channel lengths chosen were 30 mm and 35 mm. Combining these variations gives six different chips. The length of the central channel is kept constant at 50 mm and the height and width of all channels are 2 mm by 2mm. Additionally the first negative mold was designed to be casted as one piece and then separate each device post demold and cure.

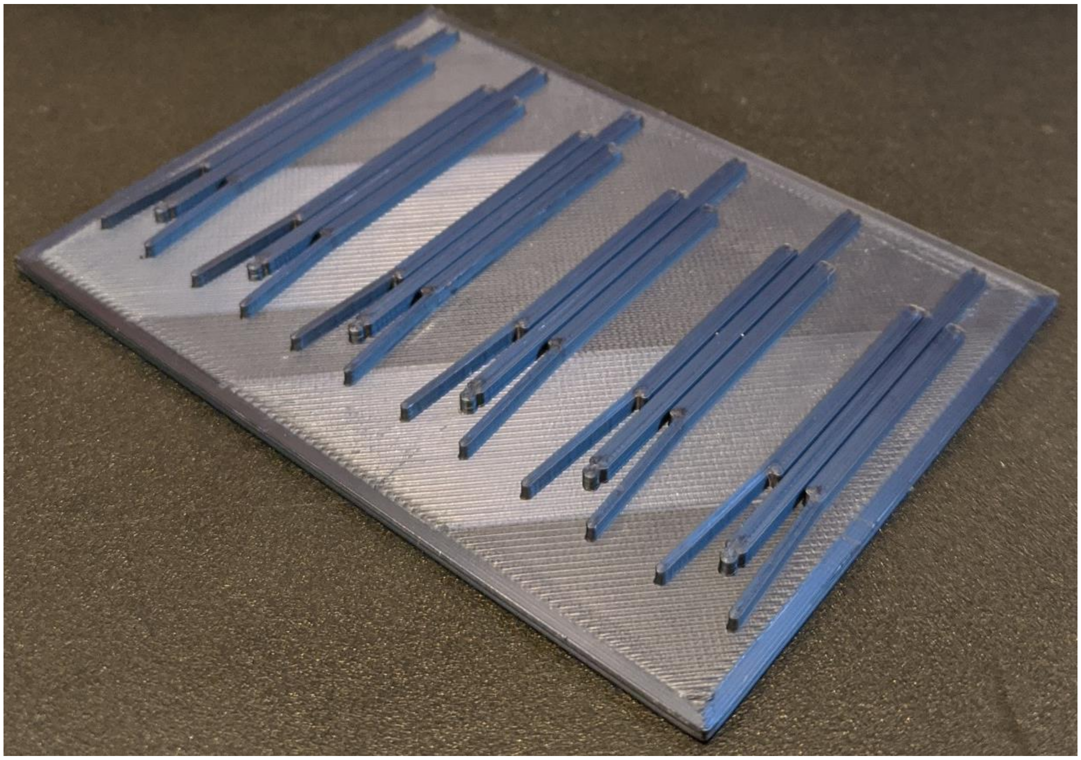

Figure 5. Proof of concept - FDM 3D printed negative mold (from right to left: 400 µm, 450 µm and 500 µm void gap and 30 mm and 35 mm pressure channel length.

The negative mold was fabricated using an FDM 3D printer out of polylactic acid (PLA) with a resolution of 0.4 mm. The negative mold is used to cast a 10:1 ratio of PDMS. Aluminum foil is used to create walls to complete the mold as shown in Figure 6. The mold and casting are placed in a free convection oven at 40 ° C for 12 hours. The temperature is kept low and therefore increasing the time to cure because of the glass transition temperature of PLA (~60° C). To demold, the cured PDMS is carefully peeled off the PLA. Holes were punched using biopsy punches for the liquid chamber inlet (1 mm diameter), liquid outlet (2 mm diameter), and the air chamber inlets (1 mm diameter). After holes were punched, the chip is bonded to a microscope slide.

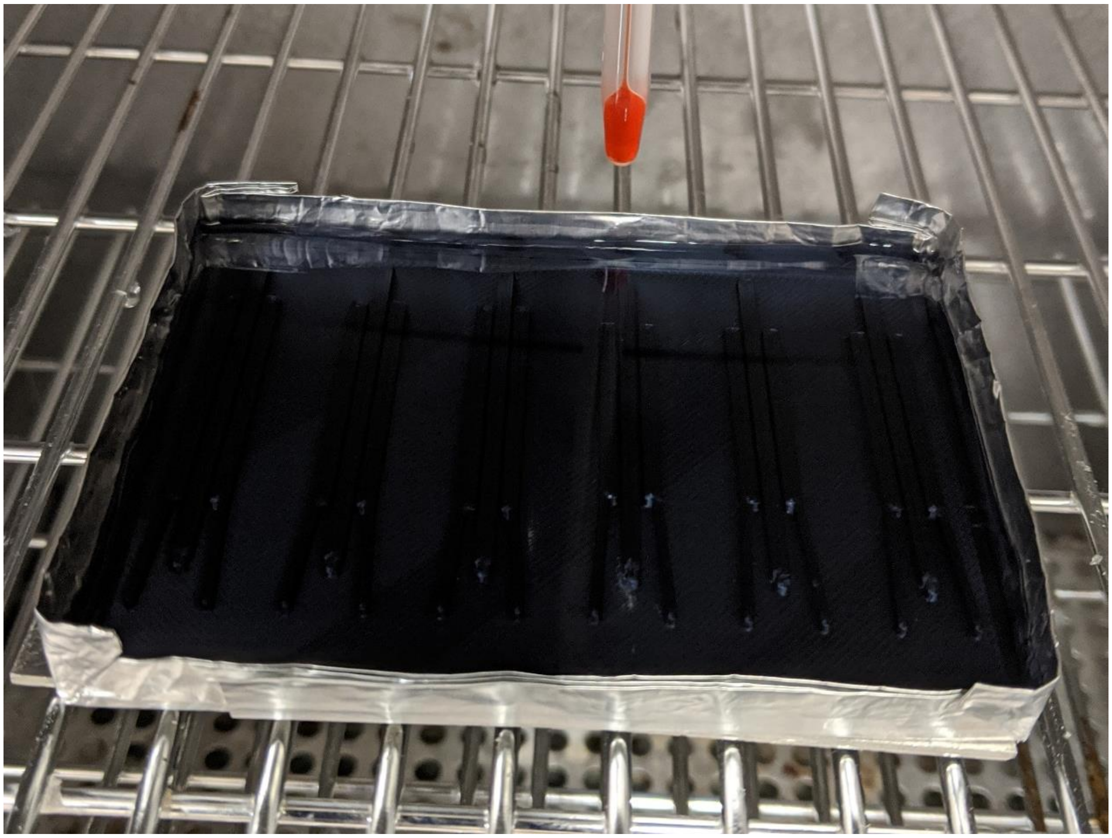

Figure 6. First mold casted with PDMS-10 and curing in free convection oven at 40° C for 12 hours.

Binding the PDMS to glass was accomplished by cleaning both surfaces and treating both surfaces with plasma. The cleaning process involves a series of 5-minute ultrasonic baths. First using ethanol, second with isopropyl alcohol, and finally with DI water. Between each bath, the chips are air dried. After cleaning, the surfaces that are to be bonded are placed face up and treated with plasma, keeping separation at 5-10 mm. Each surface receives 2.5 minutes of treatment simultaneously. The two surfaces are then placed together carefully to avoid air bubbles and bond-cured on a hotplate at 100° C for 1 hour.

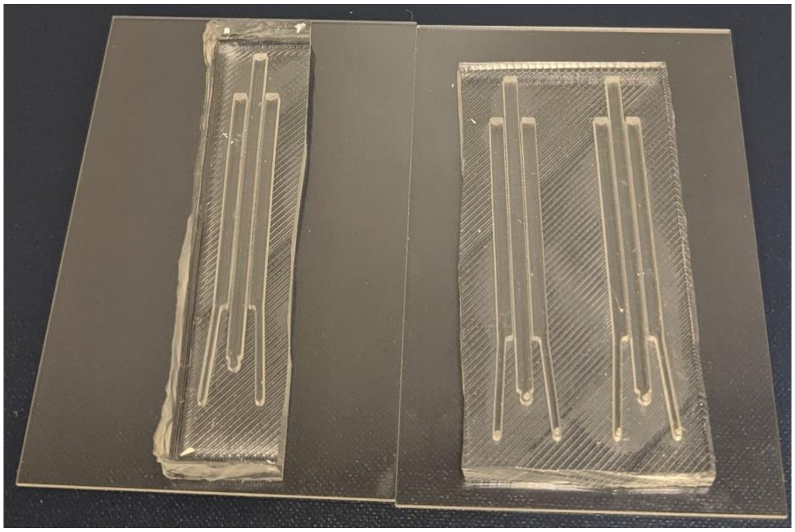

Figure 7. Completed chips, from left to right: 400 µm, 450 µm, and 500 µm. Pressure channels are 35 mm long.

To test the newly fabricated devices, a pipet tip is inserted in the central channel outlet, and we fill the central channel with dye and plug the inlet. The pressure channel inlets are attached to small hoses which are attached to a constant pressure air pump. A seal check is performed at 250 mbar of applied pressure. The failed chips can be found in Figure 8.

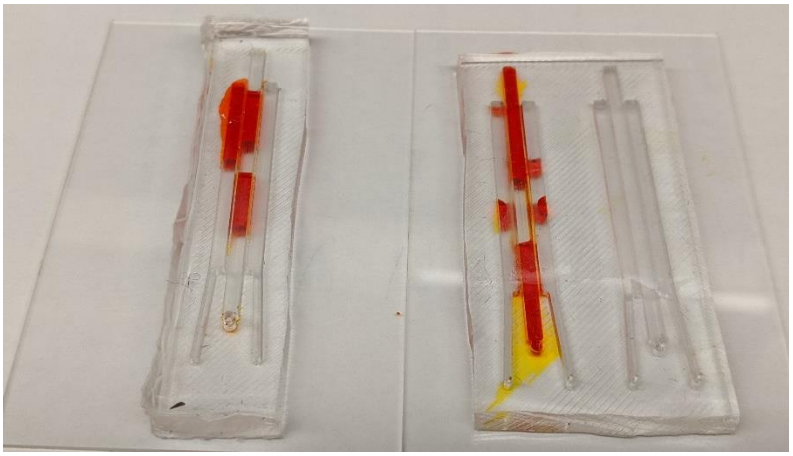

Figure 8. Failed chips – 400 µm and 450 µm have dye to show leaks. Note: the 500 µm thin wall geometry was successfully bonded.

Pressures ranging up to 300 mbar were applied and the displacement of fluid through a small pipet tip was observed. Figure 9 shows the displacement (unmeasured) of liquid in central channel subject to 300 mbar of pressure. Chip bond failure occurred when 350 mbar was applies which was evident by air bubbles forming around the bond. This is due to the high resolution of the negative mold transferring over to the PDMS layer that gets bonded to the glass slide. Despite difficulty with surface roughness, a successful binding was accomplished for a 500 µm thin wall and 35 mm pressure channel length sample chip.

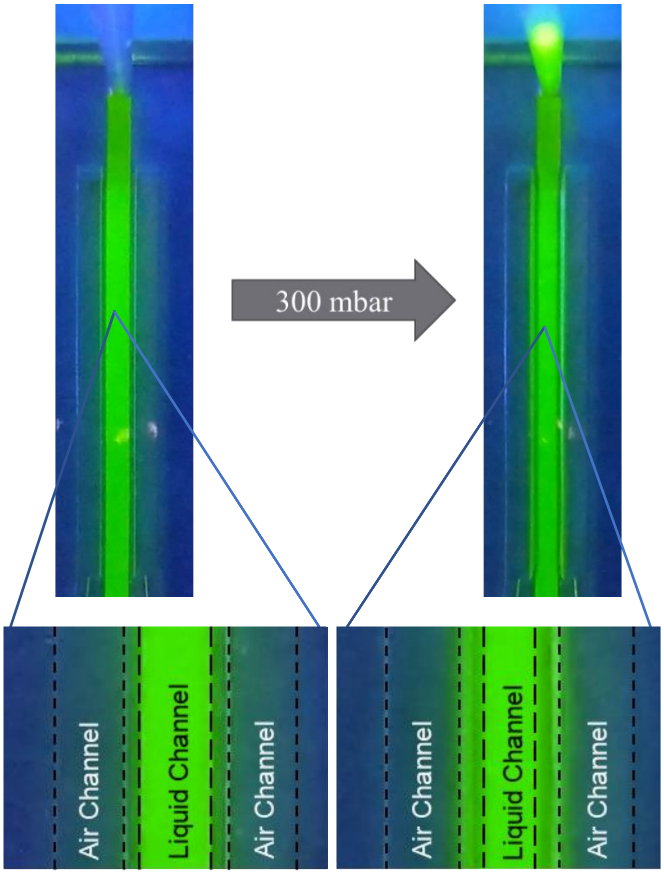

Figure 9. Before (left) and after (right) application of 300 mbar of pressure to channels on either side of central channel. FDM 3D printed, successful PDMS to glass bind (plasma treatment) - 500 µm thin wall. Bond failure was recorded on 350 mbar application.

Second negative mold design and fabrication

Improving the fabrication process was key to make this experiment work. Stereolithography (SLA) 3D printing provides resolutions much better than FDM 3D printers.

We sent our negative mold design to a 3D printing vendor and obtained molds with print resolution of 0.1 mm and a gloss finish on the top surface. The material selected was Accura-25 and was recommended by the vendor for its common use in injection molding. The gloss surface proved crucial in creating a PDMS surface bondable to glass with plasma treatment and can be seen in Figure 11.

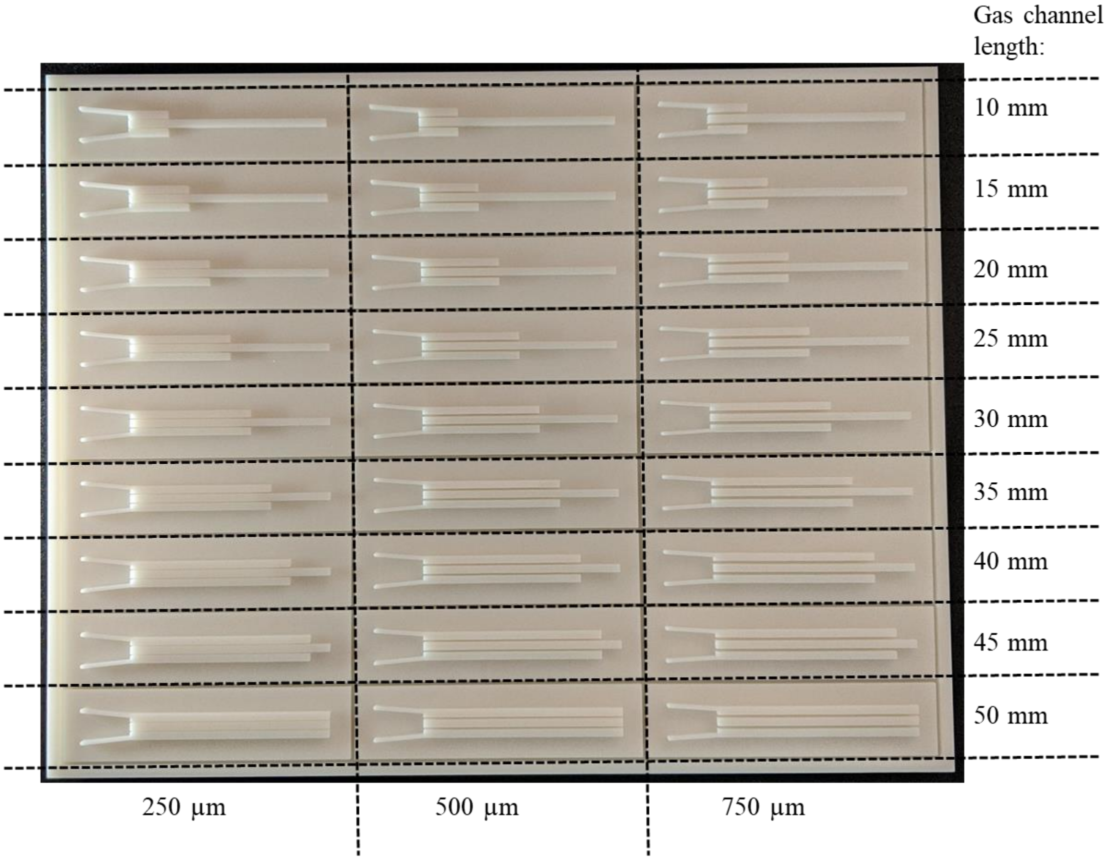

Figure 10. Array mold printed using SLA 3D printing.

Figure 11. Gloss finish of SLA 3D printed negative mold.

The pressure channel length is varied in increments of 5 mm from 50 mm down to 10 mm. The central channel length is 50 mm. The void gaps that we chose to investigate to get a broader understanding were 250 µm, 500 µm and 750 µm. Finally, instead of casting one device then splitting post cure, we decided that casting each device individually would cause less waste of PDMS and found that we could control the outside geometry better versus cutting. Figure 10 shows the geometries of the mold and discretization of each different chip.

The resultant negative mold had print failure for all the 250 µm geometries, only allowing us to investigate 500 µm and 750 µm thin wall geometries. Additionally, the mold was designed to hold several standard size microscope slides as mold walls glued together with epoxy as shown in Figure 12. The idea was pure in intent; however, the outside glass slides broke during demolding of the chips. Future mold designs will not have the lip of printed material to help secure the outside wall of glass microscope slides. In Figure 13, the damaged glass slides and the lip that causes the damage is shown

Figure 12. Mold array with installed and glued standard microscope slides (25 mm by 75 mm by 1 mm).

Figure 13. Damaged glass slides of outside walls. The lip designed to lock the glass slides in place caused the damage.

We repeated the same procedure of cleaning, plasma treating, inlet/outlet punching, and binding to glass as in the first design fabrication. These steps resulted in successful chips for 500 µm and 750 µm thin wall geometries. The only other change is that a glass capillary is used as a sight glass where the pipet tip was inserted. The glass capillary has a diameter of 1.2/2.0 mm (inner diameter/outer diameter) and is inserted so that the bottom is flush with the top of the central liquid channel. These chips were then used to help develop the experiment.

Figure 14. Completed device - second design/fabrication.

Third negative mold design and fabrication

Due to unforeseen issues with the mold from the second design, a third mold was designed and printed from the same vendor out of the same material, Accura-25. This time, however, the negative mold does not have a glossy surface finish, it is matte and has slight surface texture. The design was reduced to three chips per array and the outside support lip is removed to avoid unwanted damage to the glass slide walls. It was determined to focus on chip geometries of 500 µm, 750 µm, and 1000 µm due to print failures of the 250 µm geometries in the previous design. Additionally, focus on pressure channel lengths equal to the central channel was refined. All the channels are 50 mm long and the heights and widths remain 2 mm by 2 mm. The mold walls were glued together using epoxy. The walls consist of two printed walls with four grooves where glass slides can be inserted and glued. Once the walls are cured, they can be placed and removed from the printed base indefinitely. The mold assembly can be found in Figure 15 and Figure 16.

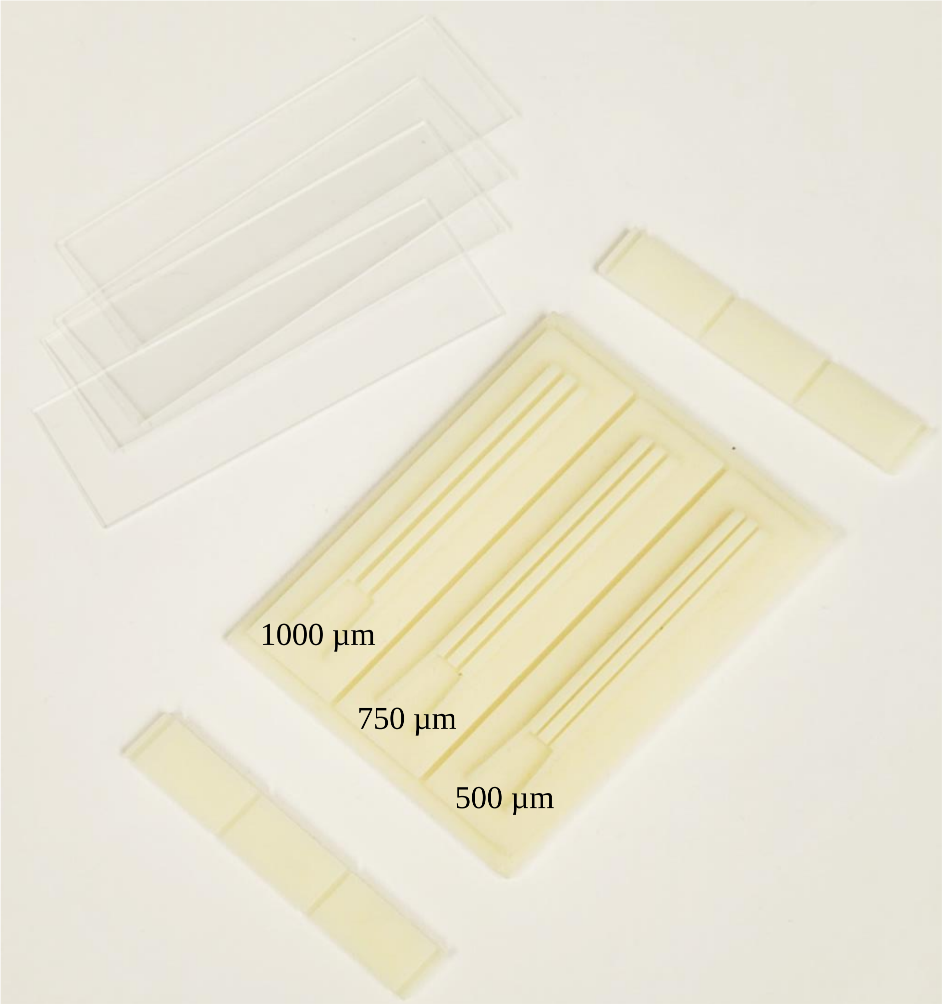

Figure 15. Third mold design consisting of the printed base, two printed sides, four standard microscope slides, and epoxy.

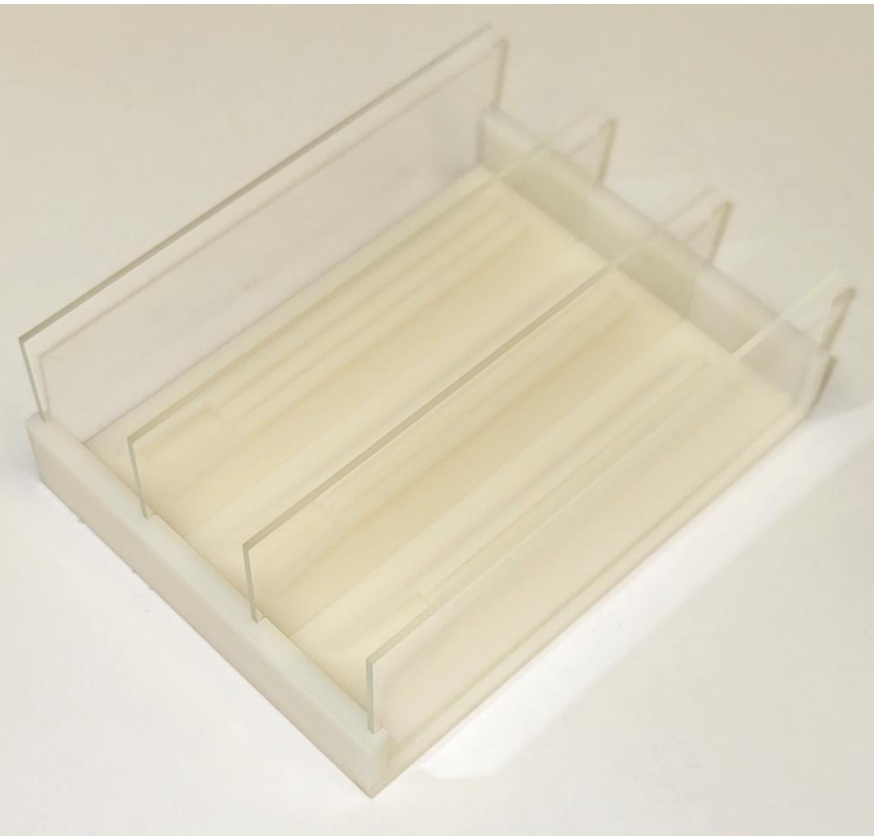

Figure 16. Completed mold of the third mold design.

Casting, demolding, punching of inlets/outlets, and plasma binding of the third design of PDMS chips is unchanged from the first and second designs. Attempts to plasma bind the resultant PDMS castings from the mold to glass slides were repeat failures. Only a small portion of the PDMS was bonding to the glass and was evident in the example shown in Figure 17. The matte, non-glossy finish of the mold is the only difference in the fabrication method.

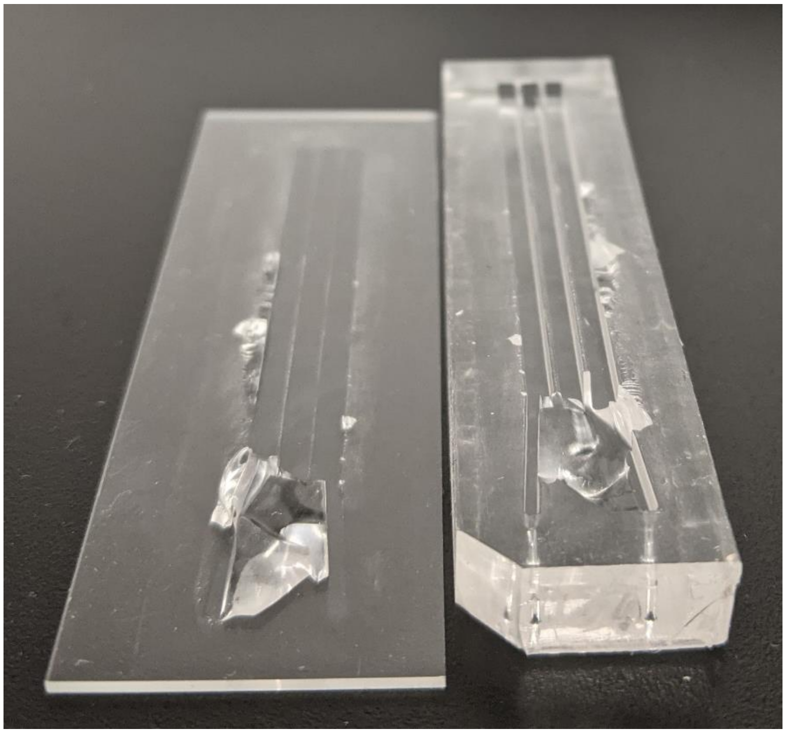

Figure 17. Example of failed plasma bond of third design.

The solution to this seeming inability to plasma bind was to employ PDMS to PDMS bonding. This method uses uncured PDMS as an adhesive to glue two pieces of PDMS together. To make use of our third design, creation of a uniform layer of PDMS was required. This is accomplished by separately spin coating PDMS for four layers and curing in between. Each layer uses 4.5 mL of PDMS and is spun at 350 RPM for 60 seconds to achieve a layer thickness of approximately 250 µm. The PDMS is applied to be spin coated using an applicator syringe and each application is completely free of air bubbles. Each layer is cured in between for 10 minutes at 60° C on a hotplate. As we increased the number of layers; SEM images revealed that there is a linear relationship as long as spin times are kept constant. Below, Figure 18 shows the linear relationship with high correlation between spin layers and overall thickness. SEM images were also taken for our smallest geometry, 500 µm, in Figure 1. Due to inability to get a capture from a known angle, we cannot get a precise measurement of the wall thickness

	Single layer	Two layers	Three layers
Thickness (μm)	241.7	424.1	757.1

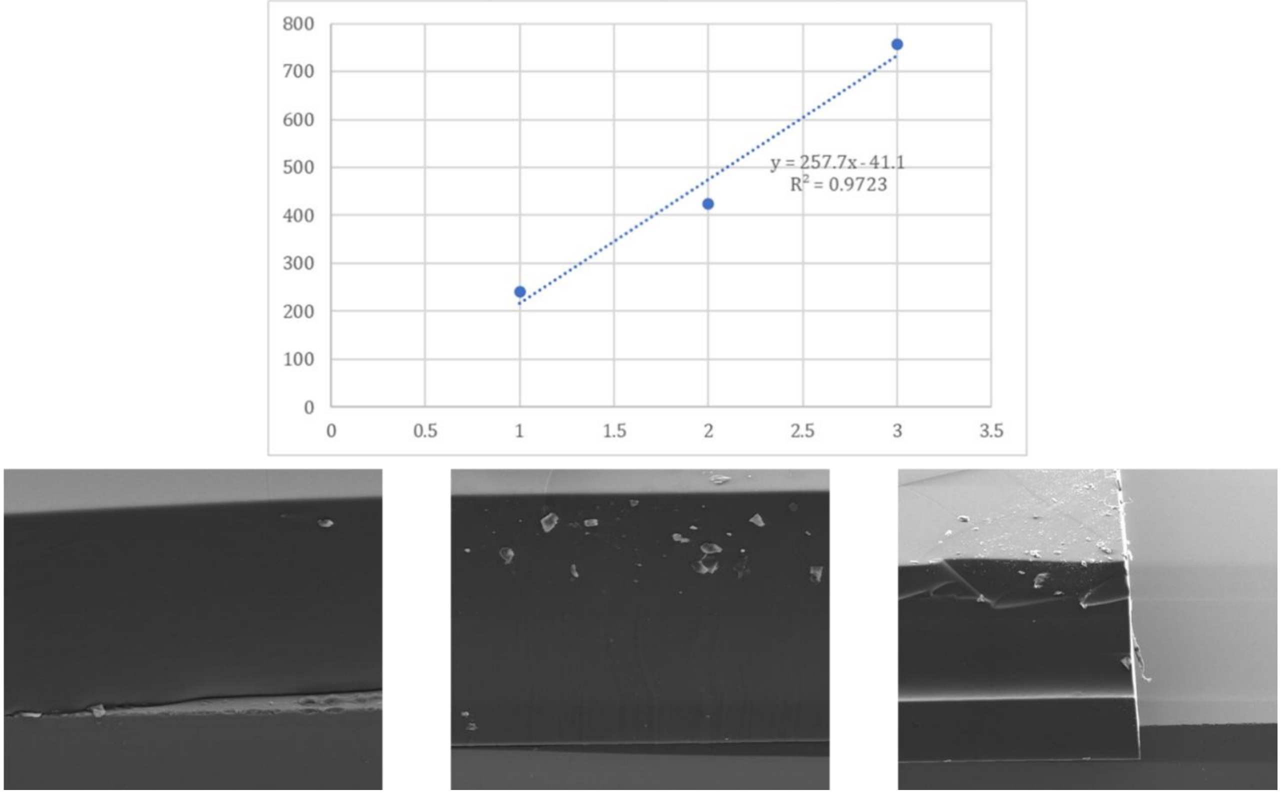

Figure 18. Top: Linear relationship of number of layers to overall thickness using spin parameters of 350 RPM for 60 seconds. Bottom: SEM images of spin coated PDMS (from left to right: 1 layer, 2 layers, and 3 layers).

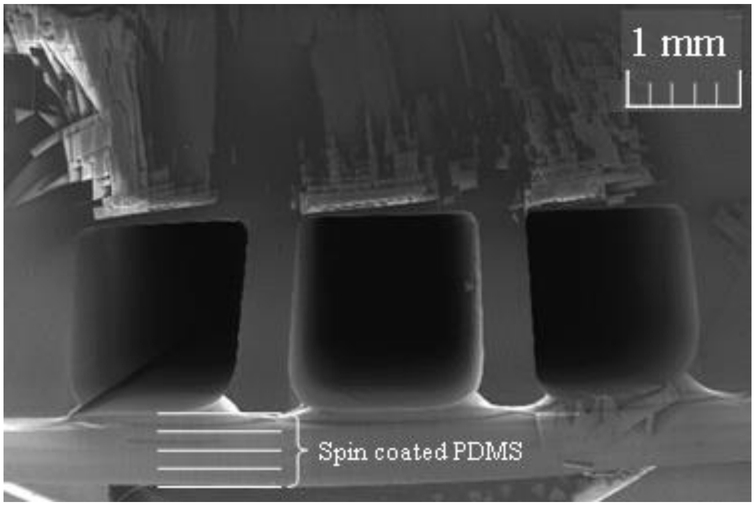

Figure 19. SEM of 500 μm thin wall. The four spin coated layers are vaguely visible.

For our chip, we decided to use a thin layer of 1 mm thickness for our PDMS layer. To achieve this, we performed the spin coating procedure stated above four times. After we have our 1 mm PDMS layer, we then spin coat another layer at 1250 RPM for 60 seconds, but do not cure it. This creates a thin film that is not visible to the naked eye. The casted PDMS is pressed onto the 1 mm layer of PDMS, and air bubbles are carefully worked to the edges. The thin film acts as an adhesive between the casted PDMS and the 1 mm layer of PDMS and the assembly is cured at 40° C in a free convection oven for 12 hours. A schematic of the PDMS-PDMS bonding is shown below, in Figure 20 and images of successful chip completions can be found in Figure 21. A slight line is visible at the bonded surfaces and there is a small amount of PDMS that pools up at the edges.

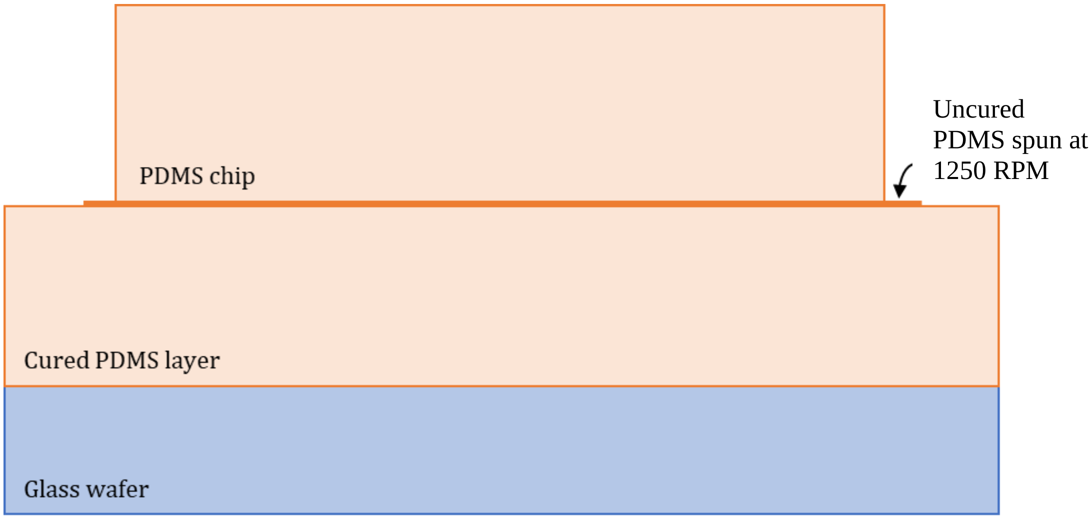

Figure 20. Schematic of a small section depicting PDMS-PDMS bonding.

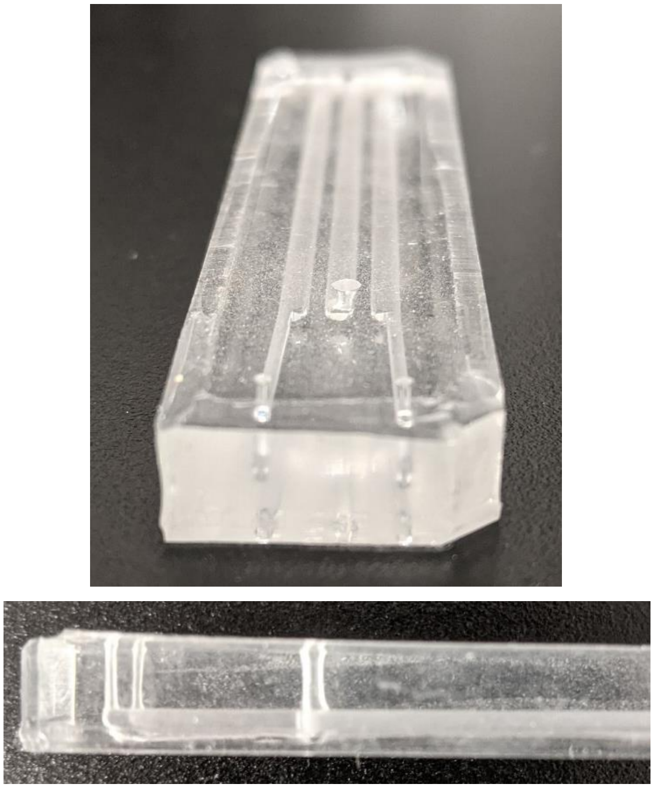

Figure 21. Successful PDMS-PDMS bonding using a thin film of uncured PDMS as an adhesive.

4.0 Data Collection

To collect data, a tabletop goniometer was used in an unorthodox way. Instead of using the stage and camera to tilt to take contact angle measurements, the stage is held stationary to capture the surface movement of liquid inside the glass capillary of the chip. The experimental setup can be referenced below, in Figure 22.

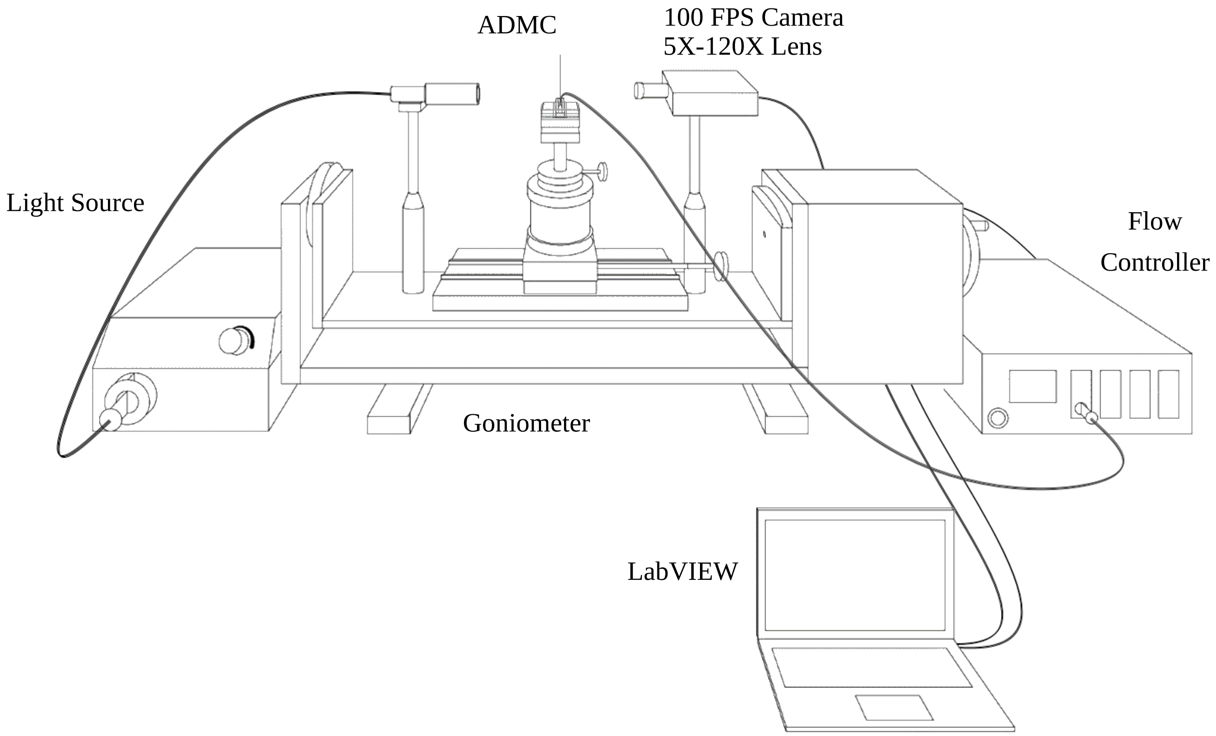

Figure 22. Illustration of experimental setup. A goniometer stage and camera is used to capture the displacement of a fluid meniscus through a capillary (Graphic credit to Sunghwan Bae).

The goniometer camera lens is replaced with a standard tabletop, c-mount, microscope lens so that a larger and more zoomed field of view may be obtained. The lens is capable of 5X-120X magnification. Manual tuning of the light source, stage location, and the magnification is how the imaging is focused. The goniometer camera is used in conjunction with an ElvFlow flow controller. The flow controller has a pressure supply resolution of 100 μbar. To synchronize data collection, a LabVIEW program was developed to control the flow controller, collect pressure data, and collect images at 60 Hz. The limitation of this program is caused by the save time of each image. Each image collected has a timestamp that corresponds to a data point in the collected pressure data.

5.0 Data Processing

To process the data, an image processing routine is employed using MATLAB. The main function of the routine uses a Canny edge detection algorithm to find distinct edges in an image [24]. The "edge" image is then cropped to omit useless data and a centroid calculation is performed. As shown in Figure 23, the image to be processed must have distinct edges and as few shades of gray as possible. The centroid calculation finds a relative pixel location to an initial height calculated before each trial. The initial height is calculated using a similar centroid process as before. To do this for thousands of frames, the process is automated to remove as much user intervention as possible by using graphical user interfacing in MATLAB.

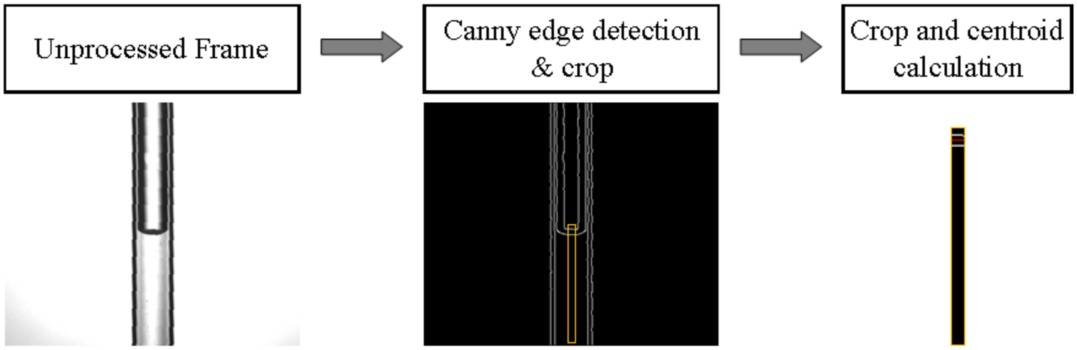

Figure 23. Image processing procedure.

Each height value is stored in a vector and saved with time and pressure for each timestamp. The result of the image processing routine are data sets with time, pressure, and height.

6.0 Results and Discussion

There were 150 trials performed in total. Of those, there were 50 trials of each geometry: 500 µm, 750 µm, and 1000 µm. And each set of 50 trials consist of 5 trials per pressure application, from 50 mbar to 500 mbar in increments of 50 mbar. Steady state responses were collected and correlated with the applied pressure and are compiled in Figure 24, Figure 25, and Figure 26. The relative heights of the responses were investigated instead of actual height because controlling the initial liquid height proved too difficult. Therefore, the raw data has varying initial heights, whereas for the relative height data, the initial heights are zero.

A strong linear trend was found between pressure application and resultant relative liquid height. The measurement error in both pressure and liquid height are very small. Very interestingly, the best fit lines are the same across each chip geometry, laying any doubt to rest that the experimental data is not qualitative. However, steady-state response isn't as interesting as the dynamic response. The entirety of the data is compiled and shown in Figure 27, Figure 28, and Figure 29. The pressure data averaged together all but yields identical responses, yielding very little error. Likewise, variation is found in the meniscus height. The grey shaded region in the meniscus height plots show the error of the averaged waveforms. Only 10 seconds is shown because the steady state is reached for each trial.

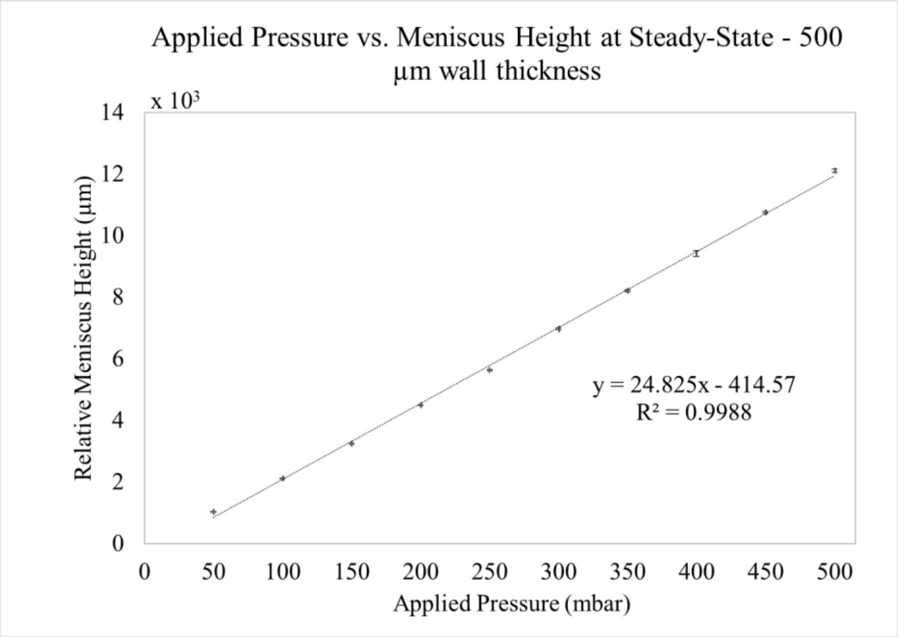

Figure 24. Steady-state response of 50 trials of pressure application and image recorded and processed liquid meniscus height for 500 µm geometry.

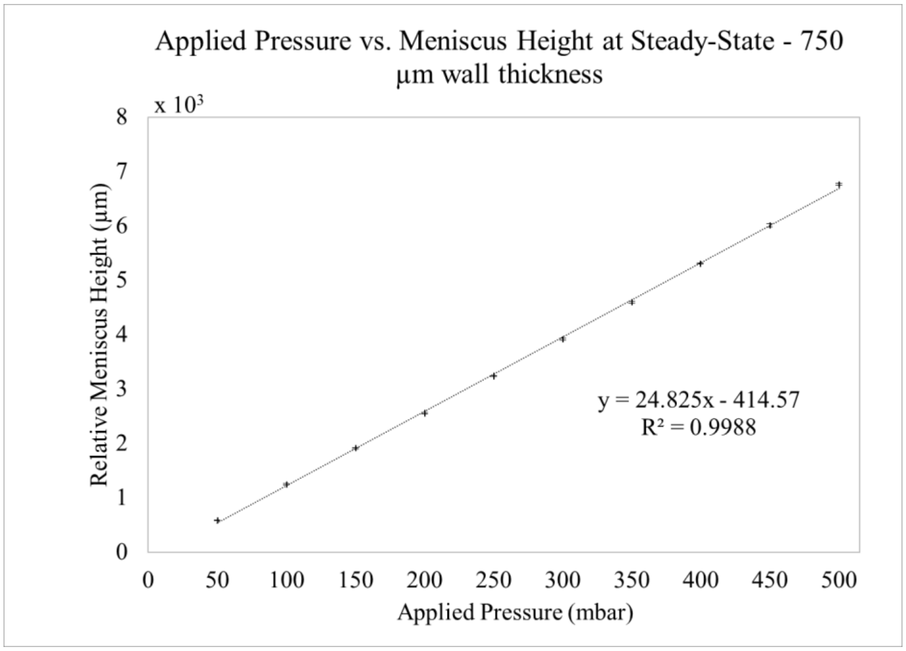

Figure 25. Steady-state response of 50 trials of pressure application and image recorded and processed liquid meniscus height for 750 µm geometry.

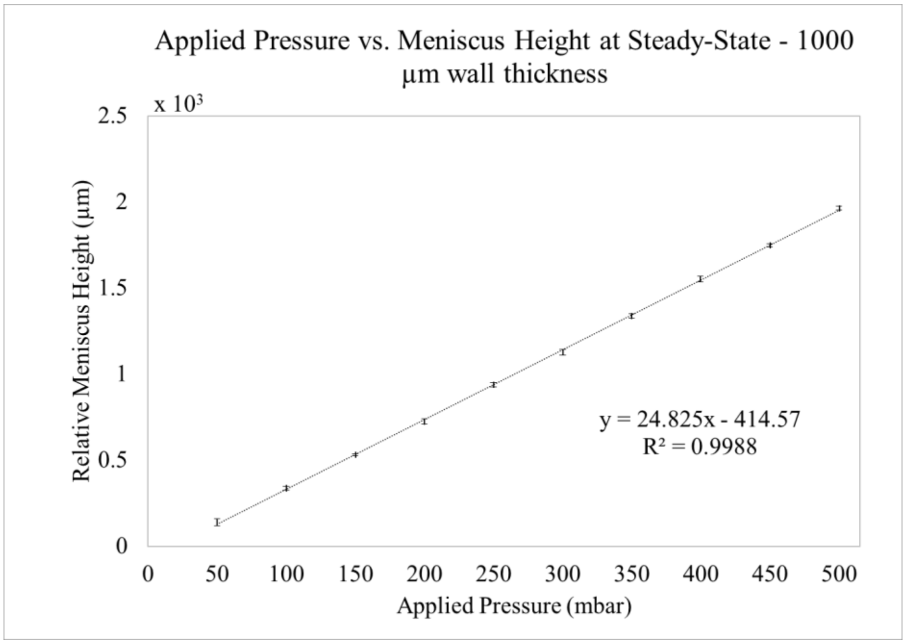

Figure 26. Steady-state response of 50 experimental trials of pressure application and image recorded and processed liquid meniscus height for 1000 µm geometry.

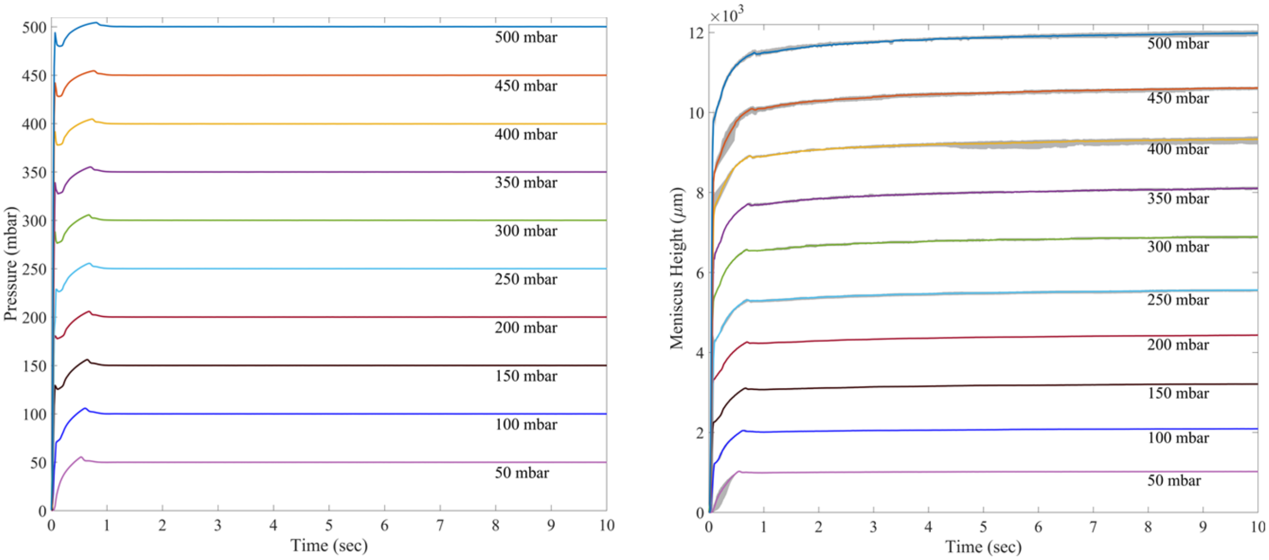

Figure 27. Experimental input pressure and output meniscus height of 500 µm.

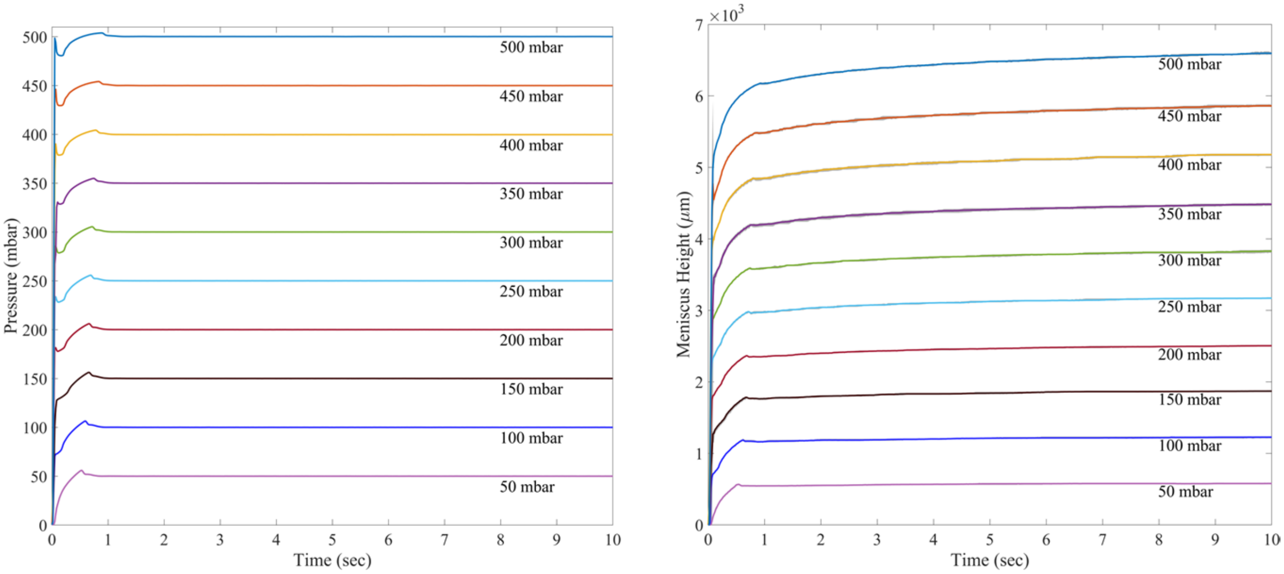

Figure 28. Experimental input pressure and output meniscus height of 750 µm.

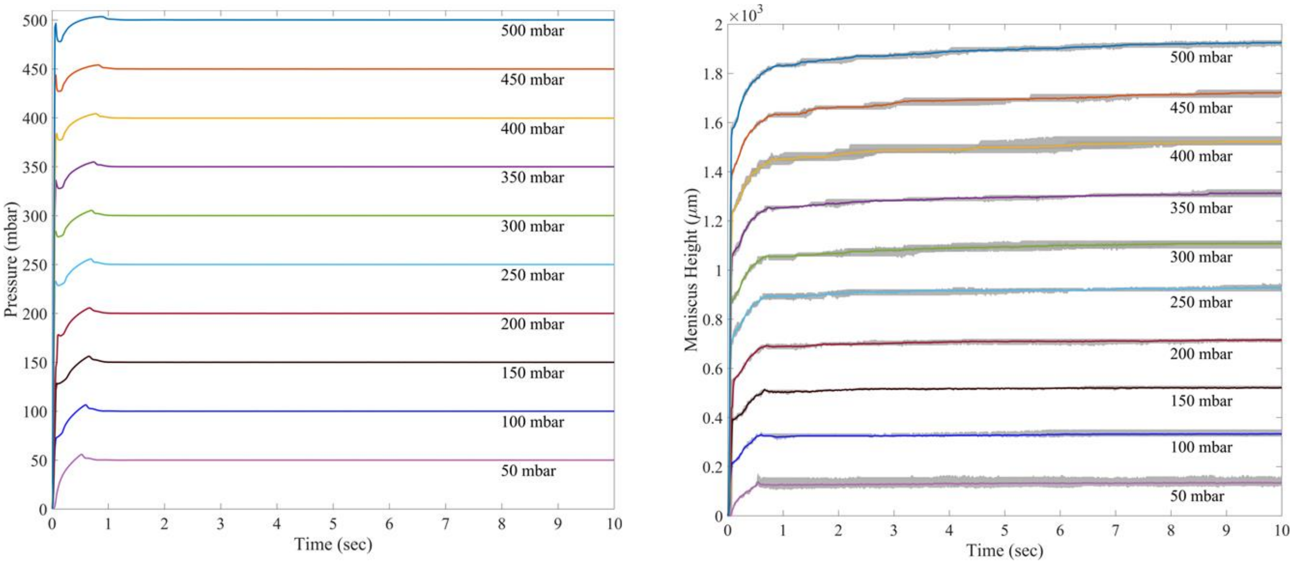

Figure 29. Experimental input pressure and output meniscus height of 1000 µm.

To simulate the experiment using the theoretical model and to generate Figure 30, Figure 31, and Figure 32, several parameters were selected and can be found below, in Table 1.

Table 2. Parameters used to simulate the theoretical model.

Wall thickness	α	P_C	f
500 mm	-92	2.2×10^4	5×10^5
750 mm	-65	6.3×10^4	8×10^5
1000 mm	-21	1.06×10^6	5×10^6

Graphical analysis indicates that there are three sequential processes that occur. First the liquid height jumps very quickly within the first 10th of a second; second the liquid gradually rises typically over the course of a half a second; finally, the liquid steadily reaches steady state which happens approximately at or before 10 seconds. The three processes can be correlated to the input pressure: where there is a steep overshoot; followed by a far less steep overshoot; then settling very quickly to steady state. These processes are evident by the abrupt changes in slope.

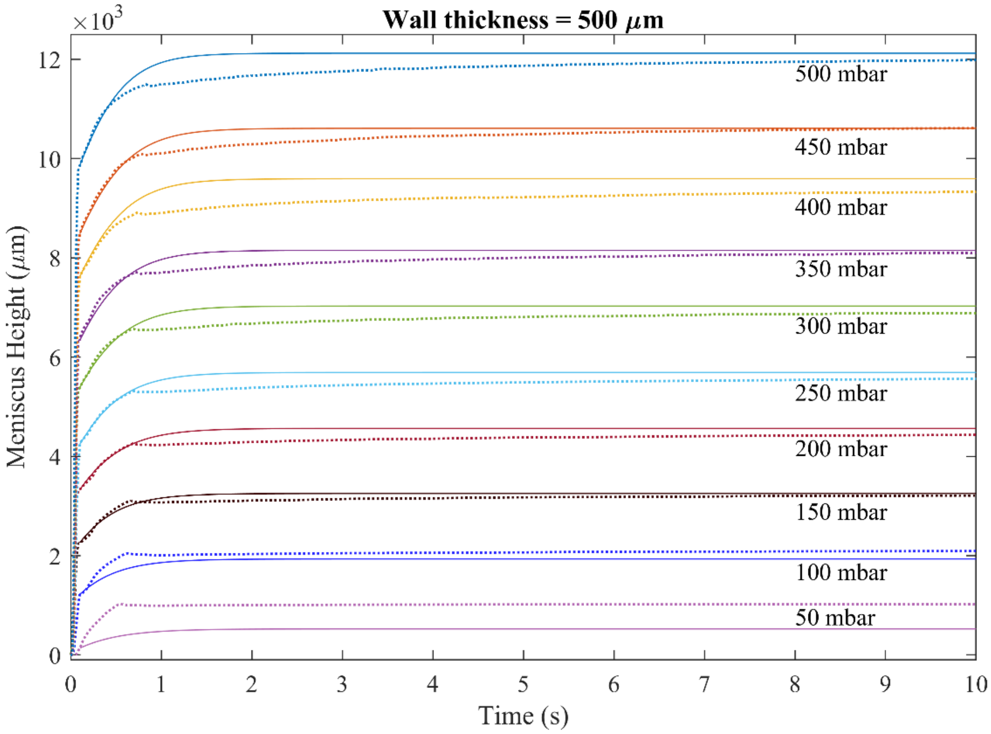

Figure 30. Experimental results (in dotted line) overlayed with simulated results (solid line) for 500 µm geometry.

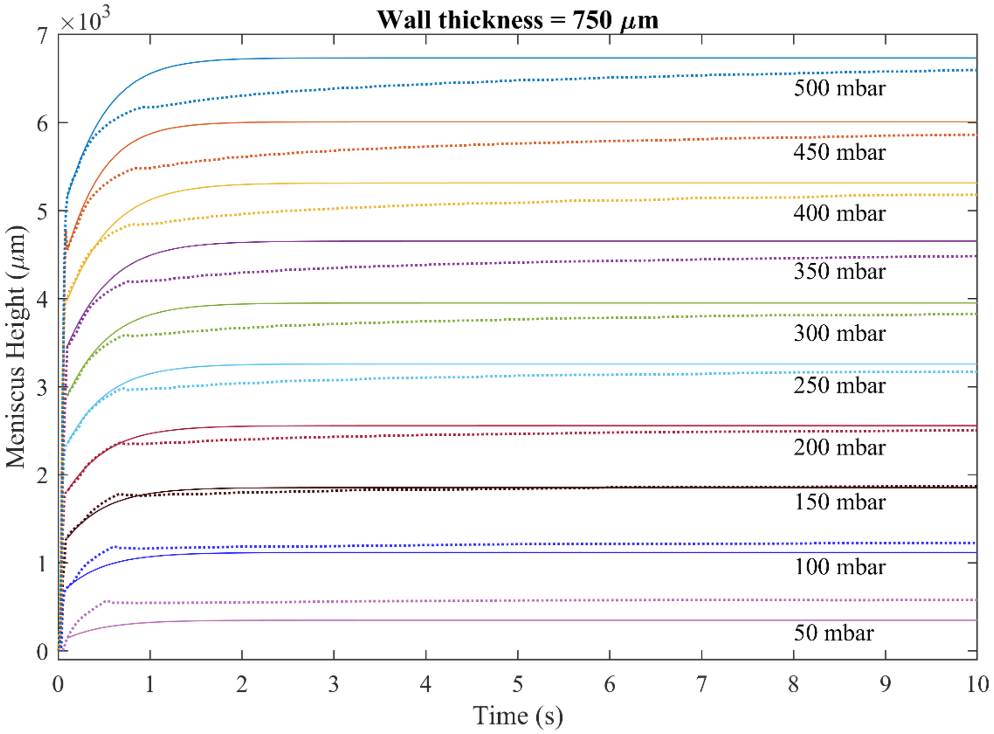

Figure 31. Experimental results (in dotted line) overlayed with simulated results (solid line) for 750 µm geometry.

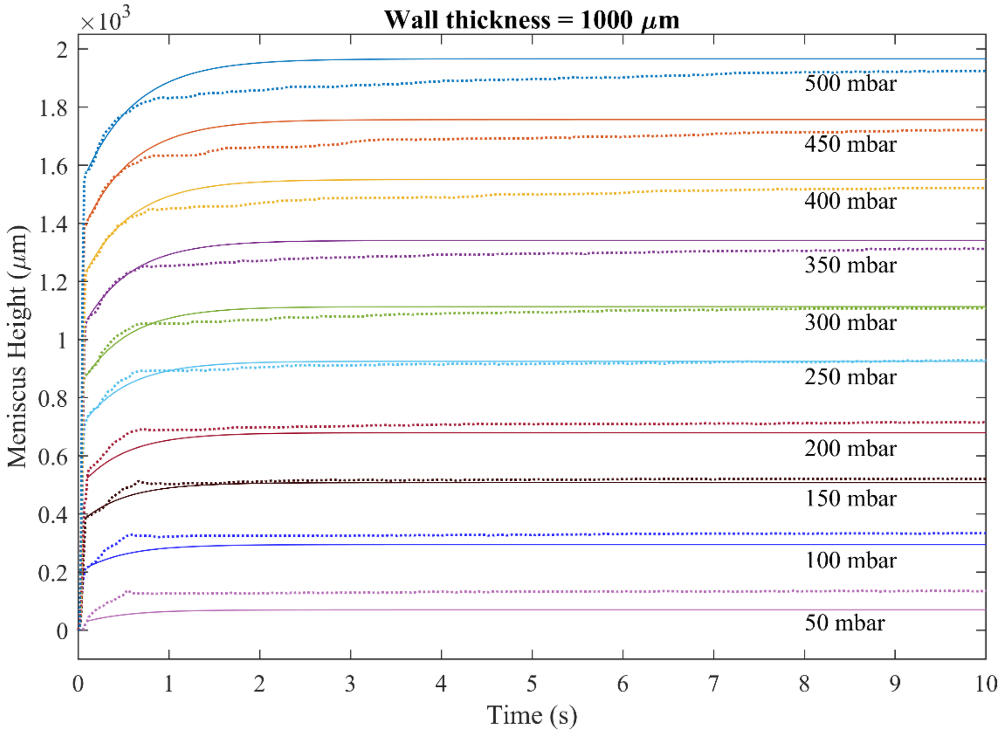

Figure 32. Experimental results (in dotted line) overlayed with simulated results (solid line) for 1000 µm geometry.

The theoretical model was unable to capture the first process of the experiment. The most likely reason for this is pre-tension during fabrication and is not describable with the theoretical model. The second process is captured well with the theoretical model. Using the height at the end of the first process as the initial height, the liquid surface height can be simulated with a very similar shape and rise time. It is perceived that the differences between the simulation are associated with the response time of the structure deformation. The theoretical model assumes uniform flow and the model does not respond as fast as the experimental result does. Non-uniformity in the overall flow may attribute to the differences.

Interestingly, the relative liquid height versus the applied pressure shows strong linear correlation as shown in Figure 24, Figure 25, and Figure 26. This strong correlation suggests that the initial height of the liquid in the capillary is negligible for small changes in height, for 12 mm or less. There is an expected trend with the parameters used in the theoretical model for simulation. The α and P_C parameters increased with channel wall thickness. This makes sense because the thicker walls lead to a stiffer cross-section. There was an unexpected change in the friction factors across the three geometries. The surface roughness should be equivalent on each chip. The irregularity of the friction factors may be attributed to the assumption that the structure has instantaneous, uniform deformation and that surface tension was not considered. Minor losses at the connection of the horizontal liquid channel and the vertical glass capillary and the total fluid mass was conserved in the model are also areas of concern. With these assumptions, the theoretical simulations match experimental results well considering the oversimplified model.

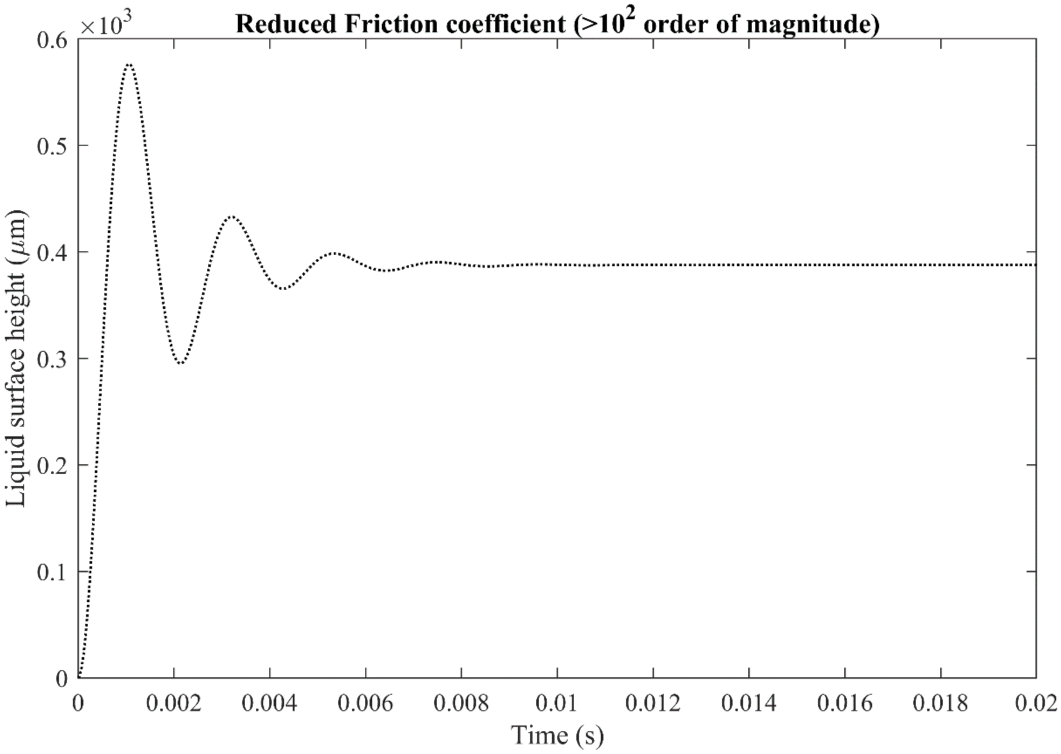

Figure 33. Reducing the friction coefficient to increase the inertial response in the flow dynamics.

Another interesting observation can be found by decreasing the friction coefficient by a few orders of magnitude. The result is a distinct overshoot and oscillation before quickly settling to steady state and is plotted in Figure 33. This result is consistent with findings in 3D computation fluid dynamic (CFD) studies of fluid flow in dentin pathways [78].

7.0 Conclusion and future work

The computational and theoretical investigation contributed new knowledge and insights on polydimethylsiloxane (PDMS) elastic polymers synthesis (including 3D stereolithography, soft lithography molding, fused deposited material and FDM 3D printed sacrificial mold), biological function and the existing material constraints, and practical solutions to address the inherent limitations. The goal was to improve the welfare of patients with dentine hypersensitivity.

Drawing from the evidence presented in the review article, PDMS-based substrates had critical drawbacks despite widespread application in microfluidics technology, biological systems engineering, and computational chemistry. The limitations included distortion following the application of external force, in-flow stream restriction, flow diversion, and pressure. The poor mechanical properties and limited chemical stability had detrimental effects on patients with dentine hypersensitivity. For example, poor chemical stability led to swelling in the presence of organic solvents. The listed drawbacks were but a microcosm of the wider challenges associated with the commercial application of PDMS. Conservative estimates indicate that more than three million persons have dentine sensitivity in the US. The condition was exacerbated by exposure to thermal stimuli such as hot beverages and foods, which led to the deformation of the dentin tubules and pressure changes in the pulp chambers.

Despite the drawbacks, the application of PDMS has grown exponentially in the past, owing to the cost and ease of production. The production of PDMS is fast, simple, and affordable compared to alternative elastic polymers, and it can be produced on a commercial scale using soft lithography. The preference for soft lithography in production and ranking as the standard fabrication methodology can be attributed to the ease of rapid prototyping of microfluidic devices and scalability. Nonetheless, the cost was initially a critical impediment; this explained why inexpensive three-dimensional (3D) printers were employed in place of expensive cleanroom facilities essential for photolithography; this led to the adoption of an affordable variant of soft lithography.

Beyond the scalable and affordable synthesis, PDMS material remains widely preferred owing to its unique material properties. For example, PDMS is clear in the visible region of the electromagnetic spectrum. Second, the material has low shrinkage rates and can easily replicate microscale features and replace plasma bonding (this phenomenon provides sufficient strength for microfluidic flow). Additionally, certain scholars have advocated for the continuous adoption of the material based on its micro-electro-mechanical systems (MEMS) and microfluidic systems and elasticity, which are superior to old-style substrate materials such as silicon, hard polymers, and glass. The contrasting observations made in the literature concerning the material-related constraints and commercial suitability suggest that addressing the existing material-related shortcomings of (PDMS) elastic polymers to resolve dentine hypersensitivity among patients in the UK remained a challenge.

The main question is whether it was practical to maintain the current status quo despite the growing demand for better-performing substrates. From an empirical perspective, the material-related constraints associated with (PDMS) elastic polymers, such as distortion with the application of external force, in-flow stream restriction, flow diversion, and pressure and performance (low thermal stability and chemical stability), outweigh the benefits (such as facile synthesis, low cost, and fast production). The observation reinforces the need for practical solutions to address the challenge.

Resolving the challenge remained a problem due to material incompatibility. On average, hydroxyapatite constitutes nearly 70% of the dentin. Developing compatible materials remained a challenge considering that dentin is opaque and hard with high-aspect-ratio micropores (1-2 µm wide); these properties make it challenging to characterize hydroxyapatite. In light of these challenges, it is clear that alternative solutions were necessary to address the problem considering it was a significant impediment to the growth of microfluidics technology and application in low-cost point of care biomedical devices, lab-on-a-chip, and micro-scale, total analysis systems. The need for better performing materials to mitigate dentine hypersensitivity informed the need to focus on PVA fibers in the next phase of research.

Future research studies should explore the following thematic issues to address the low chemical and thermal stability and distortion with the application of external force, in-flow stream restriction, flow diversion, and pressure of PDMS. Suitability of accidentally created polyvinyl alcohol-based filament extrusion using a 0.4mm FDM 3D printer nozzle has been explored. The uniformity of the diameter is about 400 ± 20 μm, if a standard 0.4 mm FDM 3D printer nozzle is used. An SEM image of the cross section a single fiber is shown in Figure 34. A novel approach is developed and should be used to improve the fabrication of a device to make a structure similar to dentin tubules. Examples are shown in Figure 35 and Figure 36. Using SLA 3D printing, a mold can be created with glass slides.

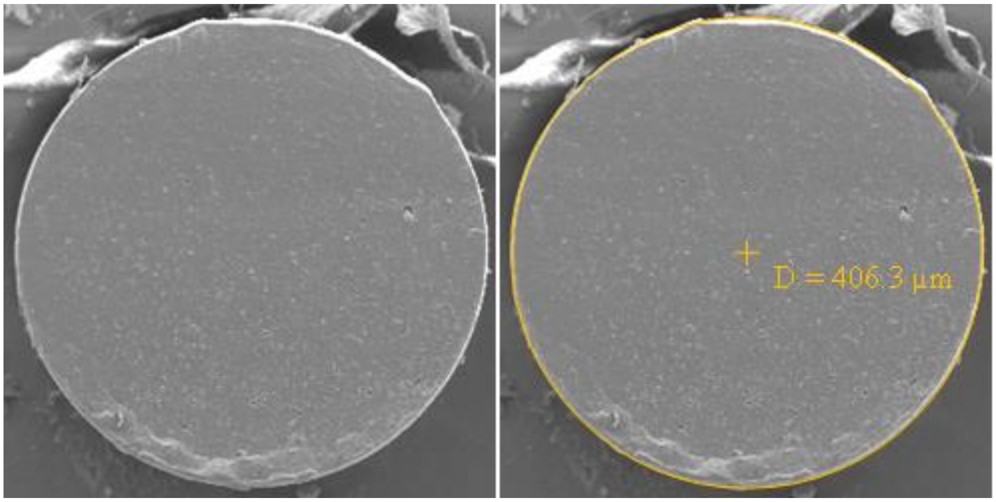

Figure 34. SEM of cross section of a PVA fiber extruded from a stainless steel 0.4 mm FDM printer nozzle at 200° C, diameter: 467 μm.

Figure 35. Planar microchip fabricated using three microfibers. Approximate spacing is between 400 – 500 µm. Food coloring is used to show discrete channels.

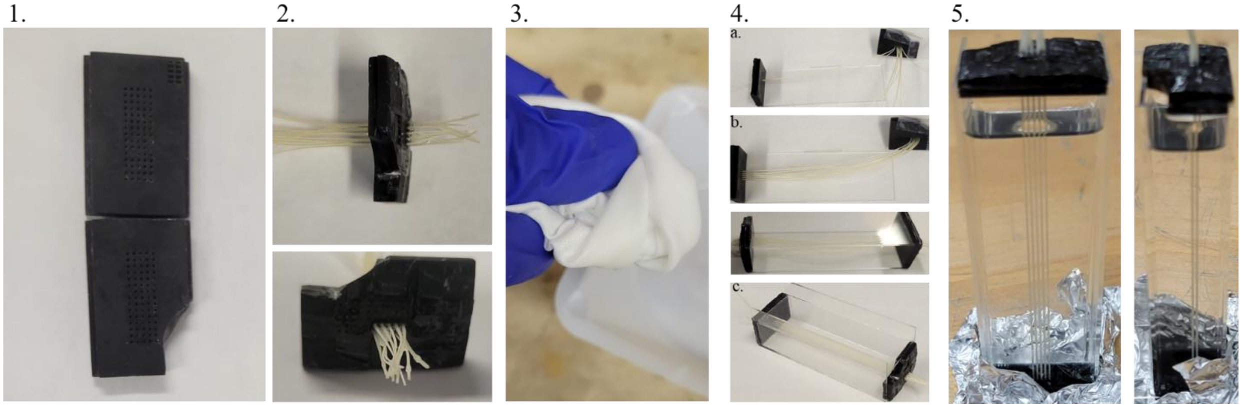

Figure 36. Assembly and casting process of new fiber design. 2 x 5 array of 400 µm diameter fibers spaced at 500 µm. 1. Cut a notch for filling the mold. 2. Fill only one end cap with fibers and glue in place. 3. Clean PVA fibers with no-residue cloth saturated with ethanol. 4. Assemble the mold: 4a. Glue an empty cap to slide with superglue. 4b. Fill the glued, empty cap with the fibers. 4c. Glue top and side slides to complete mold. 5. Fill the mold with 10:1 PDMS, vacuum treat to remove air bubbles, and then cure at 40 °C.

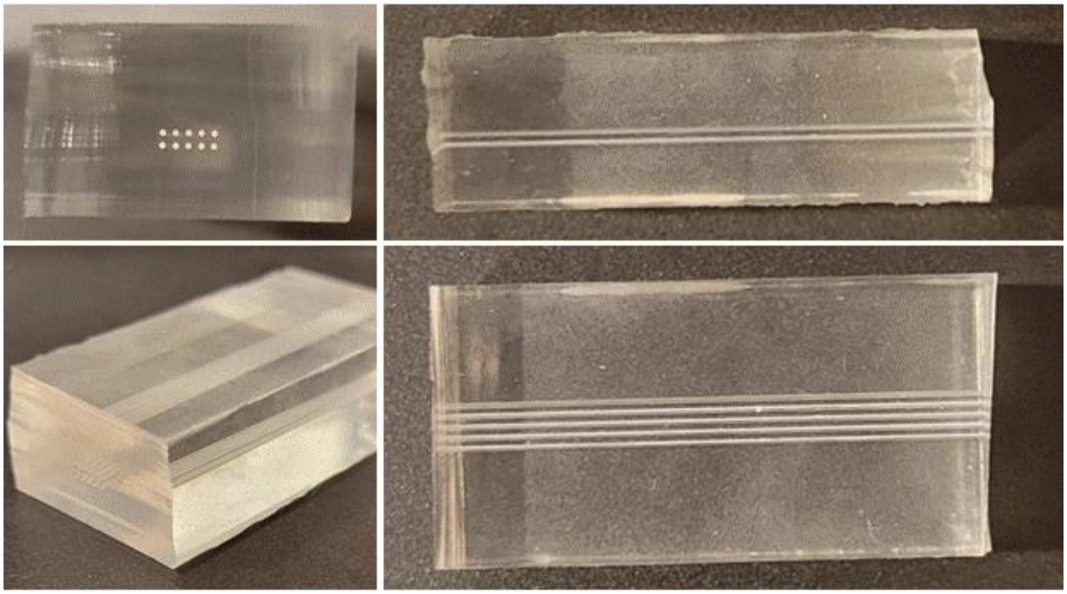

Figure 37. Competed and evacuated mold with geometry: 2 x 5 array of 400 µm diameter fibers spaced at 500 µm.

To increase correlation between the theoretical model and experiment, future work should also focus on creating a device that will better fit the tube laws. The device should be oriented so all the channels are vertical, and the devices should be one piece to help avoid losses. Additionally, the dimensions will enhance the porosity of the materials. From a theoretical point of view, it is anticipated that the yet to be developed PVA fibers would help offset the existing constraints associated with PDMS, including poor mechanical properties and limited chemical stability, and in turn, improve the quality of life of patients with dentine hypersensitivity.

8.0 References

[1] Love, R. M., and Jenkinson, H. F., 2002, “Invasion of Dentinal Tubules by Oral Bacteria,” Critical Reviews in Oral Biology & Medicine, **13**(2), pp. 171–183.

[2] Arola, D. D., Gao, S., Zhang, H., and Masri, R., 2017, “The Tooth,” Dental Clinics of North America, **61**(4), pp. 651–668.

[3] Goldberg, M., 2011, “Dentin Structure Composition and Mineralization,” Front Biosci, **E3**(2), pp. 711–735.

[4] Longridge, N. N., and Youngson, C. C., 2019, “Dental Pain: Dentine Sensitivity, Hypersensitivity and Cracked Tooth Syndrome,” Prim Dent J, **8**(1), pp. 44–51.

[5] Lin, M., Luo, Z. Y., Bai, B. F., Xu, F., and Lu, T. J., 2011, “Fluid Dynamics Analysis of Shear Stress on Nerve Endings in Dentinal Microtubule: A Quantitative Interpretation of Hydrodynamic Theory for Dental Pain,” J. Mech. Med. Biol., **11**(1), pp. 205–219.

[6] Velasco Anez, D., Hadji, C., Santanach-Carreras, E., Lorenceau, E., and Picard, C., 2021, “Microfluidic Channels of Adjustable Height Using Deformable Elastomer,” Microfluid Nanofluid, **25**(1), p. 7.

[7] Sajeesh, P., Doble, M., and Sen, A. K., 2014, “Hydrodynamic Resistance and Mobility of Deformable Objects in Microfluidic Channels,” Biomicrofluidics, **8**(5), p. 054112.

[8] Du, K., Park, M., Griffiths, A., Carrion, R., Patterson, J., Schmidt, H., and Mathies, R., 2017, “Microfluidic System for Detection of Viral RNA in Blood Using a Barcode Fluorescence Reporter and a Photocleavable Capture Probe,” Anal. Chem., **89**(22), pp. 12433–12440.

[9] Qin, P., Park, M., Alfson, K. J., Tamhankar, M., Carrion, R., Patterson, J. L., Griffiths, A., He, Q., Yildiz, A., Mathies, R., and Du, K., 2019, “Rapid and Fully Microfluidic Ebola Virus Detection with CRISPR-Cas13a,” ACS Sens., **4**(4), pp. 1048–1054.

[10] Du, K., Cai, H., Park, M., Wall, T. A., Stott, M. A., Alfson, K. J., Griffiths, A., Carrion, R., Patterson, J. L., Hawkins, A. R., Schmidt, H., and Mathies, R. A., 2017, “Multiplexed Efficient On-Chip Sample Preparation and Sensitive Amplification-Free Detection of Ebola Virus,” Biosensors and Bioelectronics, **91**, pp. 489–496.

[11] Pagella, P., Cordiale, A., Marconi, G. D., Trubiani, O., Rasponi, M., and Mitsiadis, T. A., 2021, “Bioengineered Tooth Emulation Systems for Regenerative and Pharmacological Purposes,” European Cells & Materials, **41**, pp. 502–516.

[12] Khanafer, K., Duprey, A., Schlicht, M., and Berguer, R., 2008, “Effects of Strain Rate, Mixing Ratio, and Stress–Strain Definition on the Mechanical Behavior of the Polydimethylsiloxane (PDMS) Material as Related to Its Biological Applications,” Biomed Microdevices, **11**(2), p. 503.

[13] Richmond, T., and Tompkins, N., 2021, “3D Microfluidics in PDMS: Manufacturing with 3D Molding,” Microfluid Nanofluid, **25**(9), p. 76.

[14] Lo Giudice, G., Cutroneo, G., Centofanti, A., Artemisia, A., Bramanti, E., Militi, A., Rizzo, G., Favaloro, A., Irrera, A., Lo Giudice, R., and Cicciù, M., 2015, “Dentin Morphology of Root Canal Surface: A Quantitative Evaluation Based on a Scanning Electronic Microscopy Study,” BioMed Research International, **2015**, pp. 1–7.

[15] Hossain, N., 2019, “Design and Fabrication of Deformable Microfluidic Device for the Study of Living Cells under Mechanical Solicitations,” Science & Technology Asia, **24**, p. 5462.

[16] Segletes, S. B., and Walters, W. P., 2002, “A Note on the Application of the Extended Bernoulli Equation,” International Journal of Impact Engineering, **27**(5), pp. 561–576.

[17] Wang, R.-Q., Lin, T., Shamshery, P., and Winter, A. G., V., 2016, “Control of Flow Limitation in Flexible Tubes,” Journal of Mechanical Design, **139**(1).

[18] Shapiro, A. H., 1977, “Steady Flow in Collapsible Tubes,” Journal of Biomechanical Engineering, **99**(3), pp. 126–147.

[19] Raj M, K., and Chakraborty, S., 2020, “PDMS Microfluidics: A Mini Review,” J Appl Polym Sci, **137**(27), p. 48958.

[20] Xia, Y., and Whitesides, G. M., 1998, “Soft Lithography,” Angewandte Chemie International Edition, **37**(5), pp. 550–575.

[21] McDonald, J. C., and Whitesides, G. M., 2002, “Poly(Dimethylsiloxane) as a Material for Fabricating Microfluidic Devices,” Acc. Chem. Res., **35**(7), pp. 491–499.

[22] Sollier, E., Murray, C., Maoddi, P., and Carlo, D. D., 2011, “Rapid Prototyping Polymers for Microfluidic Devices and High Pressure Injections,” Lab Chip, **11**(22), pp. 3752–3765.

[23] Johnston, I. D., McCluskey, D. K., Tan, C. K. L., and Tracey, M. C., 2014, “Mechanical Characterization of Bulk Sylgard 184 for Microfluidics and Microengineering,” J. Micromech. Microeng., **24**(3), p. 035017.

[24] Canny, J., 1986, “A Computational Approach to Edge Detection,” IEEE Transactions on Pattern Analysis and Machine Intelligence, **PAMI-8**(6), pp. 679–698.

[25] Mas, D., Espinosa, J., Roig, A. B., Ferrer, B., and Pérez, J., 2012, “Use of Subpixel Techniques in Pocket Cameras to Measure Vibrations and Displacements,” *Optics, Photonics, and Digital Technologies for Multimedia Applications II*, SPIE, pp. 232–241.

[26] Johnston, I. D., Tracey, M. C., Davis, J. B., and Tan, C. K. L., 2005, “Micro Throttle Pump Employing Displacement Amplification in an Elastomeric Substrate,” J. Micromech. Microeng., **15**(10), pp. 1831–1839.

[27] Berthier, E., Young, E. W. K., and Beebe, D., 2012, “Engineers Are from PDMS-Land, Biologists Are from Polystyrenia,” Lab Chip, **12**(7), pp. 1224–1237.

[28] Regehr, K. J., Domenech, M., Koepsel, J. T., Carver, K. C., Ellison-Zelski, S. J., Murphy, W. L., Schuler, L. A., Alarid, E. T., and Beebe, D. J., 2009, “Biological Implications of Polydimethylsiloxane-Based Microfluidic Cell Culture,” Lab Chip, **9**(15), pp. 2132–2139.

[29] Su, X., Young, E. W. K., Underkofler, H. A. S., Kamp, T. J., January, C. T., and Beebe, D. J., 2011, “Microfluidic Cell Culture and Its Application in High-Throughput Drug Screening: Cardiotoxicity Assay for HERG Channels,” J Biomol Screen, **16**(1), pp. 101–111.

[30] Lee, J. K., Park, K.-W., Choi, J. C., Kim, H.-R., and Kong, S. H., 2012, “Design and Fabrication of PMMA-Micromachined Fluid Lens Based on Electromagnetic Actuation on PMMA–PDMS Bonded Membrane,” J. Micromech. Microeng., **22**(11), p. 115028.

[31] Zhu, J., Shang, J., Brenner, D., and Lin, Q., 2013, “An Elastomeric Polymer Microchip for Mechanically Tunable Cell Trapping,” *2013 IEEE 26th International Conference on Micro Electro Mechanical Systems (MEMS)*, pp. 945–948.

[32] Ghanbari, A., Nock, V., Johari, S., Blaikie, R., Chen, X., and Wang, W., 2012, “A Micropillar-Based on-Chip System for Continuous Force Measurement OfC. Elegans,” J. Micromech. Microeng., **22**(9), p. 095009.

[33] Wu, X., Kim, S.-H., Ji, C.-H., and Allen, M. G., 2011, “A Solid Hydraulically Amplified Piezoelectric Microvalve,” J. Micromech. Microeng., **21**(9), p. 095003.

[34] Fujiwara, T., Johnston, I. D., Tracey, M. C., and Tan, C. K. L., 2010, “Increasing Pumping Efficiency in a Micro Throttle Pump by Enhancing Displacement Amplification in an Elastomeric Substrate,” J. Micromech. Microeng., **20**(6), p. 065018.

[35] “Measurement of Nonlinear Mechanical Properties of PDMS Elastomer - ScienceDirect” [Online]. Available: https://www-sciencedirect-com.ezproxy.rit.edu/science/article/pii/S0167931710005964?via%3Dihub. [Accessed: 24-Oct-2021].

[36] Wu, C.-L., Lin, H.-C., Hsu, J.-S., Yip, M.-C., and Fang, W., 2009, “Static and Dynamic Mechanical Properties of Polydimethylsiloxane/Carbon Nanotube Nanocomposites,” Thin Solid Films, **517**(17), pp. 4895–4901.

[37] Lötters, J. C., Olthuis, W., Veltink, P. H., and Bergveld, P., 1996, “Polydimethylsiloxane as an Elastic Material Applied in a Capacitive Accelerometer,” J. Micromech. Microeng., **6**(1), pp. 52–54.

[38] Lötters, J. C., Olthuis, W., Veltink, P. H., and Bergveld, P., 1997, “The Mechanical Properties of the Rubber Elastic Polymer Polydimethylsiloxane for Sensor Applications,” J. Micromech. Microeng., **7**(3), pp. 145–147.

[39] Liu, M., Sun, J., Sun, Y., Bock, C., and Chen, Q., 2009, “Thickness-Dependent Mechanical Properties of Polydimethylsiloxane Membranes,” J. Micromech. Microeng., **19**(3), p. 035028.

[40] Liu, M., Sun, J., and Chen, Q., 2009, “Influences of Heating Temperature on Mechanical Properties of Polydimethylsiloxane,” Sensors and Actuators A: Physical, **151**(1), pp. 42–45.

[41] Koschwanez, J. H., Carlson, R. H., and Meldrum, D. R., 2009, “Thin PDMS Films Using Long Spin Times or Tert-Butyl Alcohol as a Solvent,” PLoS One, **4**(2), p. e4572.

[42] Whitesides, G. M., 2006, “The Origins and the Future of Microfluidics,” Nature, **442**(7101), pp. 368–373.

[43] Yao, S., and Zhu, Y., 2015, “Nanomaterial-Enabled Stretchable Conductors: Strategies, Materials and Devices,” Advanced Materials, **27**(9), pp. 1480–1511.

[44] Eddings, M. A., Johnson, M. A., and Gale, B. K., 2008, “Determining the Optimal PDMS–PDMS Bonding Technique for Microfluidic Devices,” J. Micromech. Microeng., **18**(6), p. 067001.

[45] Shankles, P. G., Millet, L. J., Aufrecht, J. A., and Retterer, S. T., 2018, “Accessing Microfluidics through Feature-Based Design Software for 3D Printing,” PLOS ONE, **13**(3), p. e0192752.

[46] Felton, H., Hughes, R., and Diaz-Gaxiola, A., 2021, “Negligible-Cost Microfluidic Device Fabrication Using 3D-Printed Interconnecting Channel Scaffolds.,” PLoS ONE, **16**(2), p. e0245206.

[47] Guo, J., Yu, Y., Sun, L., Zhang, Z., Zhao, Y., Chai, R., and Shi, K., 2020, “Bio-Inspired Multicomponent Carbon Nanotube Microfibers from Microfluidics for Supercapacitor,” Chemical Engineering Journal, **397**, p. 125517.

[48] Lyu, Y., Yuan, X., Glidle, A., Fu, Y., Furusho, H., Yang, T., and Yin, H., 2020, “Automated Raman Based Cell Sorting with 3D Microfluidics,” Lab Chip, **20**(22), pp. 4235–4245.

[49] Lin, C.-F., Su, C.-F., Lin, K.-H., Hsieh, Y.-S., and Cheng, Y.-C., 2020, “Protein Crosslinking and Immobilization in 3D Microfluidics through Multiphoton Absorption,” ECS J. Solid State Sci. Technol., **9**(11), p. 115013.

[50] He, X., Wu, J., Hu, T., Xuan, S., and Gong, X., 2020, “A 3D-Printed Coaxial Microfluidic Device Approach for Generating Magnetic Liquid Metal Droplets with Large Size Controllability,” Microfluid Nanofluid, **24**(4), p. 30.

[51] Wang, Y., Huang, Y., Li, H., and Zhang, L., 2020, “A Convenient Plug-and-Play Coaxial Microfluidic Device and Quantitative Prediction of Monodisperse Droplets Generation,” J. Micromech. Microeng., **30**(6), p. 065009.

[52] Jeyhani, M., Thevakumaran, R., Abbasi, N., Hwang, D. K., and Tsai, S. S. H., 2020, “Microfluidic Generation of All-Aqueous Double and Triple Emulsions,” Small, **16**(7), p. 1906565.

[53] Rodriguez-Trujillo, R., Kim-Im, Y.-H., and Hernandez-Machado, A., 2020, “Controlling Shapes in a Coaxial Flow Focusing Microfluidic Device: Experiments and Theory,” Micromachines, **11**(1), p. 85.

[54] Shivhare, P. K., Bhadra, A., Sajeesh, P., Prabhakar, A., and Sen, A. K., 2016, “Hydrodynamic Focusing and Interdistance Control of Particle-Laden Flow for Microflow Cytometry,” Microfluid Nanofluid, **20**(6), p. 86.

[55] Su, R., Wen, J., Su, Q., Wiederoder, M. S., Koester, S. J., Uzarski, J. R., and McAlpine, M. C., “3D Printed Self-Supporting Elastomeric Structures for Multifunctional Microfluidics,” Science Advances, **6**(41), p. eabc9846.

[56] Goh, W. H., and Hashimoto, M., 2018, “Fabrication of 3D Microfluidic Channels and In-Channel Features Using 3D Printed, Water-Soluble Sacrificial Mold,” Macromolecular Materials and Engineering, **303**(3), p. 1700484.

[57] Goh, W. H., and Hashimoto, M., 2018, “Dual Sacrificial Molding: Fabricating 3D Microchannels with Overhang and Helical Features,” Micromachines, **9**(10).

[58] Waheed, S., Cabot, J. M., Macdonald, N. P., Lewis, T., Guijt, R. M., Paull, B., and Breadmore, M. C., 2016, “3D Printed Microfluidic Devices: Enablers and Barriers,” Lab Chip, **16**(11), pp. 1993–2013.

[59] Morgan, A. J. L., Jose, L. H. S., Jamieson, W. D., Wymant, J. M., Song, B., Stephens, P., Barrow, D. A., and Castell, O. K., 2016, “Simple and Versatile 3D Printed Microfluidics Using Fused Filament Fabrication,” PLOS ONE, **11**(4), p. e0152023.

[60] Kolesky, D. B., Truby, R. L., Gladman, A. S., Busbee, T. A., Homan, K. A., and Lewis, J. A., 2014, “3D Bioprinting of Vascularized, Heterogeneous Cell-Laden Tissue Constructs,” Advanced Materials, **26**(19), pp. 3124–3130.

[61] Femmer, T., Kuehne, A. J. C., and Wessling, M., 2014, “Print Your Own Membrane: Direct Rapid Prototyping of Polydimethylsiloxane,” Lab Chip, **14**(15), pp. 2610–2613.

[62] Bhattacharjee, N., Parra-Cabrera, C., Kim, Y. T., Kuo, A. P., and Folch, A., 2018, “Desktop-Stereolithography 3D-Printing of a Poly(Dimethylsiloxane)-Based Material with Sylgard-184 Properties,” Advanced Materials, **30**(22), p. 1800001.

[63] McDonald, J. C., Duffy, D. C., Anderson, J. R., Chiu, D. T., Wu, H., Schueller, O. J. A., and Whitesides, G. M., 2000, “Fabrication of Microfluidic Systems in Poly(Dimethylsiloxane),” ELECTROPHORESIS, **21**(1), pp. 27–40.

[64] Qin, D., Xia, Y., and Whitesides, G. M., 2010, “Soft Lithography for Micro- and Nanoscale Patterning,” Nature Protocols, **5**(3), pp. 491–502.

[65] Peter B. Howell, J., Mott, D. R., Fertig, S., Kaplan, C. R., Golden, J. P., Oran, E. S., and Ligler, F. S., 2005, “A Microfluidic Mixer with Grooves Placed on the Top and Bottom of the Channel,” Lab Chip, **5**(5), pp. 524–530.

[66] Tóth, E. L., Holczer, E. G., Ivan, K., and Fürjes, P., 2015, “Optimized Simulation and Validation of Particle Advection in Asymmetric Staggered Herringbone Type Micromixers,” Micromachines, **6**(1), pp. 136–150.

[67] “Fabrication of Fillable Microparticles and Other Complex 3D Microstructures” [Online]. Available: https://www.science.org/doi/10.1126/science.aaf7447. [Accessed: 27-Oct-2021].

[68] Kitson, P. J., Rosnes, M. H., Sans, V., Dragone, V., and Cronin, L., 2012, “Configurable 3D-Printed Millifluidic and Microfluidic ‘Lab on a Chip’ Reactionware Devices,” Lab Chip, **12**(18), pp. 3267–3271.

[69] Symes, M. D., Kitson, P. J., Yan, J., Richmond, C. J., Cooper, G. J. T., Bowman, R. W., Vilbrandt, T., and Cronin, L., 2012, “Integrated 3D-Printed Reactionware for Chemical Synthesis and Analysis,” Nature Chemistry, **4**(5), pp. 349–54.

[70] Lee, J. M., Zhang, M., and Yeong, W. Y., 2016, “Characterization and Evaluation of 3D Printed Microfluidic Chip for Cell Processing,” Microfluid Nanofluid, **20**(1), p. 5.

[71] Au, A. K., Lee, W., and Folch, A., 2014, “Mail-Order Microfluidics: Evaluation of Stereolithography for the Production of Microfluidic Devices,” Lab Chip, **14**(7), pp. 1294–1301.

[72] Dickey, M. D., Chiechi, R. C., Larsen, R. J., Weiss, E. A., Weitz, D. A., and Whitesides, G. M., 2008, “Eutectic Gallium-Indium (EGaIn): A Liquid Metal Alloy for the Formation of Stable Structures in Microchannels at Room Temperature,” Adv. Funct. Mater., **18**(7), pp. 1097–1104.

[73] Saggiomo, V., and Velders, A. H., 2015, “Simple 3D Printed Scaffold-Removal Method for the Fabrication of Intricate Microfluidic Devices,” Advanced Science, **2**(9).

[74] Kolesky, D. B., Homan, K. A., Skylar-Scott, M. A., and Lewis, J. A., 2016, “Three-Dimensional Bioprinting of Thick Vascularized Tissues,” PNAS, **113**(12), pp. 3179–3184.

[75] Miller, J. S., Stevens, K. R., Yang, M. T., Baker, B. M., Nguyen, D. T., Cohen, D. M., Toro, E., Chen, A. A., Galie, P. A., Yu, X., Chaturvedi, R., Bhatia, S. N., and Chen, C. S., 2012, “Rapid Casting of Patterned Vascular Networks for Perfusable Engineered Three-Dimensional Tissues,” Nature Materials, **11**(9), pp. 768–74.

[76] Guérin, N., Lévesque, M., and Therriault, D., 2014, “Helical Dielectrophoretic Particle Separator Fabricated by Conformal Spindle Printing,” JBiSE, **07**(09), pp. 641–650.

[77] Hwang, Y., Paydar, O. H., and Candler, R. N., 2015, “3D Printed Molds for Non-Planar PDMS Microfluidic Channels,” Sensors and Actuators A: Physical, **226**, pp. 137–142.

[78] Shirazi, M. M., Abouali, O., Emdad, H., Nabavizadeh, M., Mirhadi, H., and Ahmadi, G., 2017, “Numerical and Analytical Investigation of Irrigant Penetration into Dentinal Microtubules,” Computers in Biology and Medicine, **89**, pp. 1–17.

9.0 Supplemental Information

Fabrication procedure for Polydimethylsiloxane (PDMS) large-scale microfluidic device:

1. Preheat oven to 40 ° C.
2. Clean Accura 25 resin mold in ultrasonic bath.
   a. Two cycles with DI water.
   b. Dry with compressed air.
   c. Place magic tape over entire mold to seal dust and other debris away.
3. Pour 15 grams of PDMS per device and rigorously mix with 1.5 grams of curing agent (CA) for at least 2 minutes – timed.
4. Vacuum-treat the mixed PDMS for several minutes until all air bubbles are released.
   a. NOTE: pin sized air stream was used to release the final small bubbles that were not removed by vacuum. This is produced using a rubber bulb fitted with a pipet tip.
5. Using a 10 mL syringe, carefully apply PDMS onto mold.
6. Vacuum-treat the PDMS and mold until all the air bubbles are released.
7. Place into oven at 40 ° C for ~12 hours.
8. Remove from oven and allow PDMS and mold to cool
9. Using a thin edge, carefully remove the PDMS-to-mold bond formed on the edges of the mold.
10. Carefully peel the PDMS structure from the mold in-grain with the channels.
11. Cut the PDMS structure down to size using a fresh razor blade.

A. Binding the PDMS to glass slide for channel/device completion (glossy finish on PDMS bind surface required)

1. Clean the PDMS in ultrasonic bath.
   a. Two cycles with ethanol.
   b. Dry with compressed air.
   c. One cycle with DI water.
   d. Dry with compressed air.
   e. Place magic tape over PDMS features to keep dust and other debris out.
2. Clean the glass slides in ultrasonic bath.
   a. One cycle with acetone.
   b. Dry with compressed air.
   c. One cycle with ethanol.
   d. Dry with compressed air.
   e. One cycle with DI water.
   f. Dry with compressed air.
   g. Place magic tape over glass slide to keep dust and other debris off.
3. Treat PDMS and glass slide with plasma to ionize each surface.
   a. Remove magic tape from both the PDMS and the glass slide.

   b. Using the plasma gun, hold the tip 0.25 inches to 0.50 inches away from surfaces and treat both the glass and PDMS for 2.5 minutes simultaneously.
   c. Sparing no time, place surfaces together and squeeze to start the bond.
   d. Place on hotplate at 100 ° C with a flat weight on top for 12 hours.
   e. Remove from hot plate and cool before use.

B. Binding PDMS to PDMS for channel/device completion

1. Clean PDMS surfaces to be bonded together.
   a. Using 99% isopropyl, thoroughly rinse both surfaces.
   b. Dry surfaces with compressed air.
   c. Apply magic tape to each surface to seal away dust and debris.
2. Adhere the two surfaces.
   a. Spin coat 4.5 mL of PDMS at 1250 RPM for 60 seconds on top of lower flat surface.
   b. Gently push the upper part of the chip into the uncured PDMS film.
   c. Wiggle to remove air bubbles and to remove ensure adhesive is in contact with both surfaces entirely.

   NOTE: DO NOT vacuum treat the chip after this step. This causes large bubbles to form in the adhesive – bubbles are bad.

MATLAB video processing:

```
% Author: Chad ten Pas
% Description: This script processes a folder of images and finds the
meniscus height
% relative to a reference length in each image. It uses a canny edge
% detection that is tunable to find edges. The images are then cropped down
% to reduce data. The centroid is calculated and converted to height data.

% Update:
% (07/21/2021) Added scripting to find the initial height before pressure
% application.
%              Added pressure processing
% (08/29/2021) Added automation to select reference for pixel conversions and
% processing data.

clc,close all, clear all

filePath = 'C:\Users\chadt\Desktop\fullPDMSchip\1000um\single
outlet\800mbar\';
[~,appliedPressure,~] = fileparts(fileparts(filePath));
[~,chipGeometry,~] = fileparts(fileparts(fileparts(fileparts(filePath))));
baseDirectory = pwd;
heightFilePath = [filePath 'initialLiquidHeight\initialLiquidHeight.png'];
tic
[images,time] = readImagesToCell(filePath);
[pressure,Ptime] = readPressureToArray(filePath);
if sum(time~=Ptime) < 1
    clear Ptime
    %delete this later
    fprintf('Both time vectors are identical!\n\n')
    heightImage = imread(heightFilePath);
    [actualLiquidHeight,angleRotated] = imageProcess(heightImage,images);
    smoothedLiquidHeight = smooth(actualLiquidHeight,'moving');
    relativeTime = seconds(time - time(1));

    fig1 = figure('Position',[60,460,2400,600]);
    set(fig1,'defaultAxesColorOrder',[0,0,0;0,0.4470,0.7410])
    set(gca,'TickLabelInterpreter','latex','FontSize',14)
    set(0,'defaulttextInterpreter','latex');
    yyaxis left
    plot(relativeTime,pressure)
    ytl = get(gca, 'YTick'); % Get Controlling Left Ticks
    ylabel('Pressure
(mbar)','FontSize',16,'rotation',0,'HorizontalAlignment','right')
    yyaxis right
    set(0,'defaulttextInterpreter','latex');
    plot(relativeTime,smoothedLiquidHeight,'LineWidth',1.25)
    ytr = get(gca, 'YTick'); % Get Right Tick Values
    ytrv = linspace(min(ytr), max(ytr), numel(ytl)); % Create New Right Tick
Values Matching Number Of Left Ticks
    ytrc = compose('%.0f',ytrv); % Tick Label Cell Array
    set(gca, 'YTick',ytrv, 'YTickLabel',ytrc)
    grid on, grid minor
```

```
    ylabel('Meniscus displacement
($\mu$m)','FontSize',16,'rotation',0,'HorizontalAlignment','left')
    xlabel('time (s)','FontSize',16)
    title([chipGeometry, ' thin wall subject to
',appliedPressure],'FontSize',22)


savefig(fig1,[baseDirectory,'/processed/',chipGeometry,'_',appliedPressure,'.
fig']);

hgexport(fig1,[baseDirectory,'/processed/',chipGeometry,'_',appliedPressure,'
.png'],hgexport('factorystyle'), 'Format', 'png')

save([baseDirectory,'/processed/',chipGeometry,'_',appliedPressure,'.mat'],'r
elativeTime','pressure','actualLiquidHeight','smoothedLiquidHeight')
else
    fprintf('There is an inconsistancy in your time vectors, please
resolve.\n\n')
end
toc

% FUNCTIONS
function [imagesCell,timeArray] = readImagesToCell(filePath)
%% Reads *.PNG images from a folder directory and puts them into a cell
array.
% Inputs:
%   filePath = the folder directory of the *.PNG images. In the
%   format of 'C:\*\Folder\'
% Outputs:
%   imagesCell = all the images placed in a cell array.
%   timeArray = vector of time when the images were created.

imageFiles = dir([filePath '*.png']);
nFiles = length(imageFiles);    % Number of files found
for i = 1 : nFiles
    currentFilename = imageFiles(i).name;
    temp = currentFilename(5:27);
    timeArray(i) = datetime(temp,'InputFormat','yyyy-MM-dd HH-mm-
ss.SSS','Format','yyyy-MM-dd HH-mm-ss.SSS');
    currentImage = imread([filePath currentFilename]);
    imagesCell{i} = currentImage;
end
imagesCell = imagesCell';
timeArray =  timeArray';
end

function [pressureArray,PtimeArray] = readPressureToArray(filePath)
%% Reads the pressure & time data from a folder directory and puts them into
a array.
% Inputs:
%   filePath = the folder directory with the . In the
%   format of 'C:\*\Folder\'
% Outputs:
%   PressureArray = vector of pressure data.
%   PtimeArray = vector of time corresponding to pressure data.
pressureFile = [filePath 'press_data'];
```

```
tempTable = readtable(pressureFile);
pressureArray = tempTable{:,1};
PtimeArray = datetime(tempTable{:,2},'InputFormat','yyyy-MM-dd_HH-mm-
ss.SSS','Format','yyyy-MM-dd_HH-mm-ss.SSS');
end

function [actualLiquidHeight,angleRotated] =
imageProcess(heightImage,theImages)
initialLiquidHeight = getInitialLiquidHeight(heightImage,2000);
[edgeImages] = edgeImageCell(theImages);
[angleRotated,rotatedImages] = autoRotateImageCell(edgeImages);
pixelConversionFactor = getPixelConversion(rotatedImages{1},2000);
[~,croppedImages] = autoCropImageCell(rotatedImages);
pixelHeight = getPixelHeight(croppedImages);
actualLiquidHeight = pixelHeight * pixelConversionFactor +
initialLiquidHeight;
end

%% Functions
function initialLiquidHeight =
getInitialLiquidHeight(heightImage,knownReferenceDistance)

t1 = edge(heightImage,'Canny',[.1 .4]);
fig1 = figure('Name','getInitialLiquidHeight: Select the bottom of the
chip.','NumberTitle','off');
[bottom,bottomrect] = imcrop(t1);
close(fig1)
fig1 = figure('Name','getInitialLiquidHeight: Select the
meniscus.','NumberTitle','off');
[top,toprect] = imcrop(t1);
close(fig1)

props = regionprops(true(size(bottom)),bottom, 'WeightedCentroid');
bottomLoc = bottomrect(2) + props.WeightedCentroid(2);

props = regionprops(true(size(top)),top, 'WeightedCentroid');
topLoc = toprect(2) + props.WeightedCentroid(2);

pixelHeight = bottomLoc - topLoc;

% get the conversion to calculate actual height
fig1 = figure('Name','getInitialLiquidHeight(getPixelConversion): Select left
line to analyze (first line going from left will be
used).','NumberTitle','off');
[~,leftrect] = imcrop(t1);
close(fig1)

fig1 = figure('Name','getInitialLiquidHeight(getPixelConversion): Select
right line area to analyze (first line going from left will be
used).','NumberTitle','off');
[~,rightrect] = imcrop(t1);
close(fig1)
leftrect = round(leftrect);
rightrect = round(rightrect);
leftline = imcrop(t1,leftrect);
```

```
rightline = imcrop(t1,rightrect);
[~,leftInd] = find(leftline(1,:)~=0);
[~,rightInd] = find(rightline(1,:)~=0);
rightPixel = rightrect(1) + rightInd;
leftPixel = leftrect(1) +leftInd;
pixelWidth = rightPixel - leftPixel;
pixelConversionFactor = knownReferenceDistance/pixelWidth;
initialLiquidHeight = pixelHeight * pixelConversionFactor;
end

function [edgeImages] = edgeImageCell(theImages)
nImages = length(theImages);
for i = 1:nImages
    edgeImages{i} = edge(theImages{i},'Canny',[.2 .6]);
end
edgeImages = edgeImages';

end

function pixelConversionFactor =
getPixelConversion(edgeImage,knownReferenceDistance)
% finds the pixel conversion factor of an image by using two crop cuts.
fig1 = figure('Name','getPixelConversion: Select left line to analyze (first
line going from left will be used).','NumberTitle','off');
[~,leftrect] = imcrop(edgeImage);
close(fig1)

fig1 = figure('Name','getPixelConversion: Select right line area to analyze
(first line going from left will be used).','NumberTitle','off');
[~,rightrect] = imcrop(edgeImage);
close(fig1)
leftrect = round(leftrect);
rightrect = round(rightrect);
leftline = imcrop(edgeImage,leftrect);
rightline = imcrop(edgeImage,rightrect);
[~,leftInd] = find(leftline(1,:)~=0);
[~,rightInd] = find(rightline(1,:)~=0);
pixelWidth = rightrect(1)+rightInd(1) - leftrect(1)+leftInd(1);
pixelConversionFactor = knownReferenceDistance/pixelWidth;
end

function pixelHeight = getPixelHeight(croppedImages)
%% Finds the pixelheight of the meniscus reletive to the initial meniscus
height.
nImages = length(croppedImages);
props = regionprops(true(size(croppedImages{1})), croppedImages{1},
'WeightedCentroid');
verticalCentroidFirst = props.WeightedCentroid(2);
for i = 1:nImages
   props = regionprops(true(size(croppedImages{i})), croppedImages{i},
'WeightedCentroid');
   verticalCentroid = props.WeightedCentroid(2);
   pixelHeight(i) = verticalCentroid - verticalCentroidFirst;
end
pixelHeight = -pixelHeight;
% interpolate out the NaN entries
```

```
xvals = 1:1:length(pixelHeight);
pixelHeight = interp1(xvals,pixelHeight,xvals,'makima');
pixelHeight = pixelHeight';
end

function [angleToRotate,rotatedImages] = autoRotateImageCell(theImages)
%% Calculates the angle of corrrection using the first frame and then applies it to the rest of the images.
% Calculate the angle of corrrection using the first frame
nImages = length(theImages);
fig1 = figure('Name','autoRotateImageCell: Select area to analyze (left-most line will be analyzed).','NumberTitle','off');
[croppedImage,rect] = imcrop(theImages{1});
close(fig1)
% get the first line in first row
[~,topInd] = find(croppedImage(1,:)~=0);
topInd = topInd(1);
% get the first line in last row
[~,bottomInd] = find(croppedImage(end,:)~=0);
bottomInd = bottomInd(1);
% get the height of the two reference points
verticalDist = length(croppedImage(:,1));
% calculate angle of correction
if bottomInd == topInd
    angleToRotate = 0;
elseif bottomInd < topInd
    angleToRotate = atand((topInd-bottomInd)/verticalDist);
elseif bottomInd > topInd
    angleToRotate = -atand((bottomInd-topInd)/verticalDist);
end
% Apply rotation to images.
for i = 1:nImages
    rotatedImages{i} = imrotate(theImages{i},angleToRotate);
end
rotatedImages = rotatedImages';

end

function[rectCrop,croppedImages] = autoCropImageCell(theImages)

nImages = length(theImages);
fig1 = figure('Name','autoCropImageCell: Select the area to analyze (meniscus & capillary).','NumberTitle','off');
[~,rect] = imcrop(theImages{1});
close(fig1)
rect = round(rect);
firstImage = theImages{1};

for i = 1:nImages
    croppedImages{i} = imcrop(theImages{i},rect);
end
croppedImages = croppedImages';
rectCrop = rect;
end
```

LabVIEW data acquisition, video acquisition, and flow control Virtual Interface (.VI):

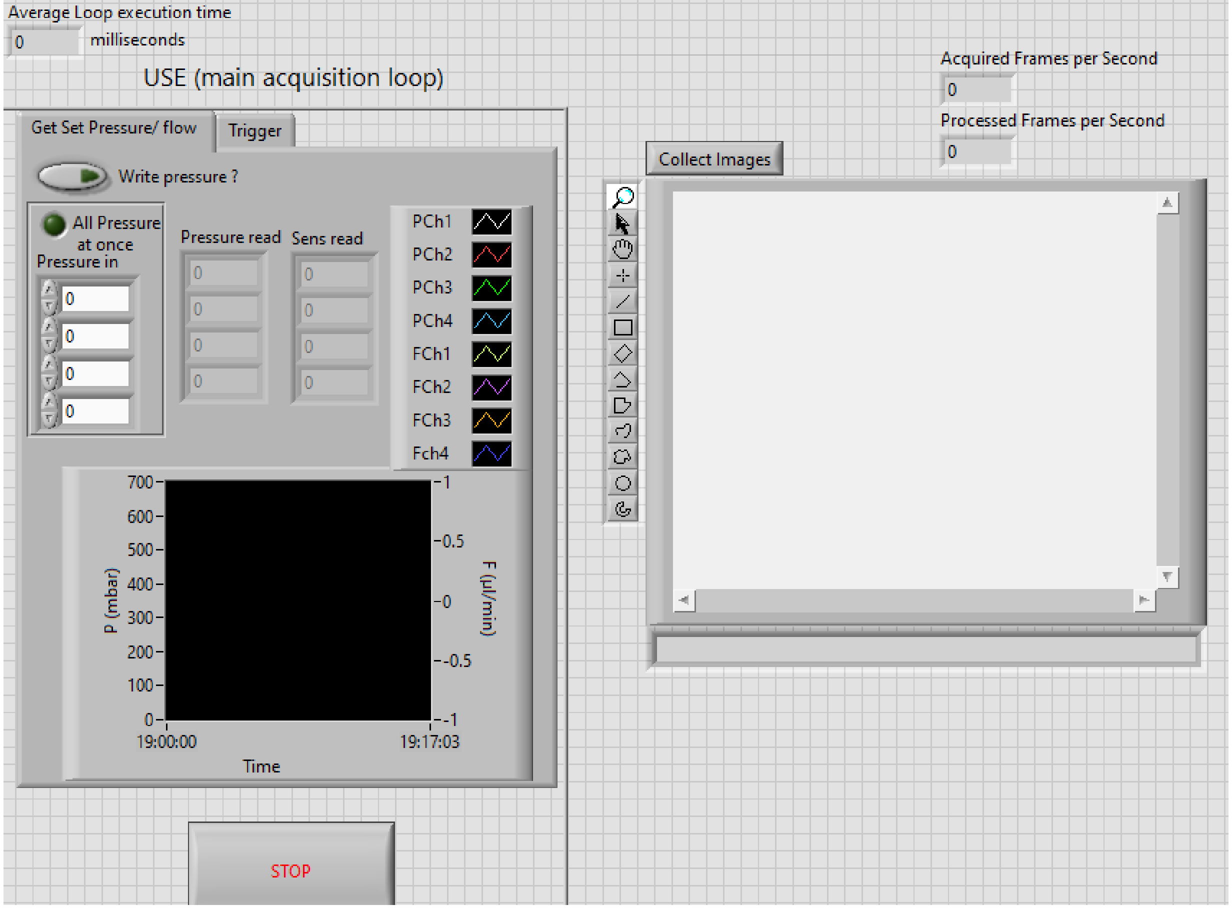

Average Loop execution time 0 milliseconds

Acquired Frames per Second 0

Processed Frames per Second 0

Figure 38. LabVIEW front panel interface used to control the presser controller and collect pressure data and images. Note: only the first channel is used in the main acquisition loop.